

DRAFT VERSION JULY 30, 2022

Typeset using L^AT_EX preprint style in AASTeX62A *Chandra* X-ray Survey of Optically Selected AGN PairsMEICUN HOU,^{1,2,3} ZHIYUAN LI,^{1,2} AND XIN LIU^{3,4}¹*School of Astronomy and Space Science, Nanjing University, Nanjing 210046, China*²*Key Laboratory of Modern Astronomy and Astrophysics (Nanjing University), Ministry of Education, Nanjing 210046, China*³*Department of Astronomy, University of Illinois at Urbana-Champaign, Urbana, IL 61801, USA*⁴*National Center for Supercomputing Applications, University of Illinois at Urbana-Champaign, 605 East Springfield Avenue, Champaign, IL 61820, USA*

ABSTRACT

We present a *Chandra* archival study of optically selected AGN pairs at a median redshift $\bar{z} \sim 0.1$. Out of 1286 AGN pairs (with projected separations $r_p < 100$ kpc and velocity offsets $\Delta v < 600$ km s⁻¹) optically identified from the Sloan Digital Sky Survey Seventh Data Release, we find 67 systems with archival *Chandra* observations, which represent the largest sample of optically selected AGN pairs studied in the X-ray. Among the 67 AGN pairs, 18 systems have both nuclei detected in the X-rays, 39 have one nucleus detected in the X-rays, whereas 10 have no X-ray detection. The X-ray detection rate, $75/134=56\%(\pm 6\%$ 1σ Poisson errors), is significantly higher than that ($23/134=17\%\pm 4\%$) of a comparison sample of star-forming galaxy pairs, lending support to the optical AGN classification. In the conservative case where X-ray contamination from star formation is removed, the X-ray detection rate becomes $27\%\pm 4\%$, consistent with predictions from latest galaxy merger simulations. The 2–10 keV X-ray luminosity $L_{2-10 \text{ keV}}$ increases with decreasing projected separation in AGN pairs for $r_p \gtrsim 15$ kpc, suggesting an enhancement of black hole accretion even in early-stage mergers. On the other hand, $L_{2-10 \text{ keV}}$ appears to decrease with decreasing projected separation at $r_p \lesssim 15$ kpc, which is contradictory to predictions from merger simulations. The apparent decrease in $L_{2-10 \text{ keV}}$ of AGN pairs at $r_p \lesssim 15$ kpc may be caused by: (i) enhanced absorbing columns from merger-induced gas inflows, (ii) feedback effects from early-stage mergers, and/or (iii) small number statistics. Future X-ray studies with larger samples are needed to put our results on firmer statistical ground.

Keywords: black hole physics – galaxies: active – galaxies: interactions – galaxies: nuclei – X-rays: galaxies

houmc@smail.nju.edu.cn

lizy@nju.edu.cn

xinliuxl@illinois.edu

1. INTRODUCTION

Galaxy mergers and close interactions have long been recognized to have played a vital role in shaping the structure and morphology of galaxies (e.g., Zwicky 1956; Vorontsov-Velyaminov 1959; Toomre & Toomre 1972; Khachikian 1987; Sanders et al. 1988; Barnes & Hernquist 1992) and particularly the cores of ellipticals (e.g., Faber et al. 1997; Graham 2004; Merritt et al. 2004; Lauer et al. 2005; Kormendy et al. 2009). They are thought to drive accretion in the central supermassive black holes (SMBHs; Hernquist 1989; Norman & Scoville 1988; Moore et al. 1996; Ciotti & Ostriker 2007; Ciotti et al. 2010), fueling at least some Active Galactic Nuclei (AGNs). However, the causal link between galaxy interactions and AGNs has been highly controversial. The details of AGN feeding, and in particular, the role of mergers, may be radically different at high and low accretion rates (e.g., Ho 2008; Treister et al. 2012; Hopkins et al. 2014; Villforth et al. 2017; Donley et al. 2018).

One fundamental question in the study of AGNs is the mechanism for triggering their growth. For quasars (i.e., high-luminosity AGNs), one hypothesis is that they are triggered by gas-rich major mergers between galaxies (the “merger hypothesis”; Sanders & Mirabel 1996; Kauffmann & Haehnelt 2000; Hopkins et al. 2008). In the hierarchical Λ CDM paradigm, small structures merge to form large structures, and the merger rate of dark matter halos peaks at early times (Bell et al. 2006), in broad consistency with the observed peak of bright quasar activities (e.g., Richards et al. 2006). Gas-rich major mergers (i.e., those between galaxies of comparable mass and with plenty of gas) provide an efficient mechanism for channelling a large amount of gas into the central region, triggering starbursts and rapid black hole growth (e.g., Hernquist 1989; Mihos & Hernquist 1996; Di Matteo et al. 2005). Observationally, the merger hypothesis is supported by the connection between quasars and ultra-luminous infrared galaxies (ULIRGs; e.g., Sanders & Mirabel 1996), by signatures of recent mergers in quasar hosts (e.g., Bahcall et al. 1997; Bennert et al. 2008), and by the small-scale over-densities of galaxies around luminous quasars and quasar pairs (e.g., Bahcall et al. 1997; Serber et al. 2006; Hennawi et al. 2006; Myers et al. 2008; Shen et al. 2010). While these observations do not necessarily prove that mergers are directly responsible for quasar triggering, they suggest that quasar activity is coincident with mergers in many cases. Indeed, merger-based phenomenological models can reproduce virtually all the statistical properties of quasars (e.g., Hopkins et al. 2008; Shen 2009).

However, at lower AGN luminosities (i.e., $L_{\text{bol}} \lesssim 10^{45} \text{ erg s}^{-1}$), the causal link between mergers and AGN triggering has been elusive. Some observations found an excess of close neighbors in AGN host galaxies or a higher fraction of AGNs in interacting than in isolated galaxies (e.g., Petrosian 1982; Hutchings & Campbell 1983; Dahari 1984; Kennicutt & Keel 1984; Keel et al. 1985; Bahcall et al. 1997; Serber et al. 2006; Koss et al. 2010; Silverman et al. 2011; Ellison et al. 2011; Liu et al. 2012) whereas others detected no significant difference (e.g., Dahari 1985; Schmitt 2001; Miller et al. 2003; Grogin et al. 2005; Waskett et al. 2005; Pierce et al. 2007; Ellison et al. 2008; Li et al. 2008; Darg et al. 2010; Villforth et al. 2014, 2017). Because less fuel is required, secular processes such as instabilities driven by bars and minor mergers, may be sufficient to trigger low-luminosity AGNs (e.g., Hopkins et al. 2014; Menci et al. 2014). One important goal in AGN studies is to distinguish between different fueling routes, i.e., violent major-mergers versus secular processes, and to assess their relative contributions as functions of redshift and AGN luminosity.

Binary SMBHs are thought to be a generic outcome in the hierarchical paradigm of structure formation (Begelman et al. 1980; Milosavljević & Merritt 2001; Yu 2002), given that most massive galaxies harbor SMBHs (Kormendy & Richstone 1995; Richstone et al. 1998). Binary SMBHs have

long been proposed theoretically (e.g., Begelman et al. 1980; Milosavljević & Merritt 2001; Yu 2002; Merritt 2013), invoked to explain a variety of phenomena, such as the core properties of elliptical galaxies (e.g., Faber et al. 1997; Kormendy et al. 2009), “X”-shaped radio morphologies (e.g., Merritt & Ekers 2002), peculiar AGN broad emission line profiles (e.g., Gaskell 1982; Boroson & Lauer 2009; Shen & Loeb 2010; Eracleous et al. 2012; Shen et al. 2013; Liu et al. 2014; Wang et al. 2017), quasi-periodic flux variabilities in AGNs (e.g., Graham et al. 2015a,b; D’Orazio et al. 2015). Both SMBHs in a merger may accrete at the same time, which will be observable as a pair of AGNs (also being referred to as “dual AGNs” for pairs with separations < 10 kpc; for a recent review, see De Rosa et al. 2020). However, it is difficult to predict when one and in particular both SMBHs become active (e.g., Shlosman et al. 1990; Armitage & Natarajan 2002; Wada 2004; Dotti et al. 2007, 2012; Blecha et al. 2013). Observations of AGN pairs help understand galaxy mergers in general and tidally-triggered AGN in particular. Their host-galaxy properties offer clues to the external and internal conditions under which both SMBHs are activated at the same time.

Large, homogeneous optical surveys such as the Sloan Digital Sky Survey (SDSS) have increased the inventory of AGN pairs on tens-of-kpc to kpc scales by more than an order of magnitude. At high redshift ($z > 0.5$), quasar pair candidates can be selected from imaging data and confirmed by follow-up spectroscopy. Due to the moderate imaging resolution and the relatively high redshift, most SDSS quasar pairs are on $>$ tens-of-kpc scales (e.g., tens of systems known with ~ 50 – 100 kpc (projected separation) at $0.5 < z < 5$; Hennawi et al. 2006, 2010; Shen et al. 2010; Vignali et al. 2018). However, these quasar pairs are still relatively far away from each other; it is unclear that their host galaxies are in direct tidal interactions with each other or not, except in rare cases where tidal tails are seen using deep imaging at the low-redshift end (e.g., Green et al. 2010). At lower redshift ($z < 0.5$), AGN pairs can be found at smaller physical separations where direct tidal interactions between their host galaxies are more likely.

However, studies based on large ($> 10^3$ pairs), optical AGN pair samples are hampered by the use of $[\text{O III}]$ luminosity as an AGN luminosity surrogate. $[\text{O III}]$ comes from the narrow-line regions which are thought to reside outside the dusty torus (Antonucci 1993); there is a large scatter (~ 1 dex) between $[\text{O III}]$ luminosity and the intrinsic AGN luminosity (e.g., Heckman et al. 2005; Panessa et al. 2006; Lamastra et al. 2009). In contrast, X-rays come from the corona much closer to the SMBH and accretion disk, providing arguably the most direct evidence for AGN. In particular, the hard X-ray (2–10 keV) band is transparent to column densities of $N_{\text{H}} \lesssim 10^{24}$ and is powerful to reveal obscured AGNs except in Compton-thick sources. *Chandra* was instrumental in discovering the prototypical dual AGN in the ULIRG NGC 6240 (Komossa et al. 2003; Tananbaum et al. 2014), whose nuclei are heavily obscured in the optical and are characteristic of LINERs (Lutz et al. 1999); another example is the dual AGN in Mrk 266 (Mazzarella et al. 2012). Similarly, many nuclei in the optically selected AGN pair sample of Liu et al. (2011b) have line ratios characteristic of LINERs or composites, which may be driven by stellar or shock heating (e.g., Lutz et al. 1999; Terashima et al. 2000; Yan & Blanton 2012). X-rays provide the most unambiguous tracer of AGNs. Previous X-ray studies, however, are limited to relatively small samples of local ULIRGs or Swift BAT AGNs (e.g., Teng et al. 2012; Koss et al. 2012, 2016) which represent the low-luminosity AGN population in nearby galaxies. The main challenge in X-ray studies is the need for a statistically large sample that covers a wide dynamical range in spatial separations.

In this paper, we present an X-ray study of a parent sample of 1286 [O III]-selected (including both type 1s, i.e., unobscured and type 2s, i.e., obscured) AGN pairs at redshift $z \sim 0.1$ matched against the *Chandra* X-ray data archive. Our targets were optically selected from the SDSS DR7 (Abazajian et al. 2009) by Liu et al. (2011b) which represent the largest sample of optically selected AGN pairs. Both the nuclei of each of these galaxy mergers are optically classified as type 2 or type 1 AGNs¹. The optical classification for the two nuclei is based on their individual optical spectra from the SDSS, which exhibit optical diagnostic emission line ratios indicative of AGN (including both Seyferts and LINERs) and/or AGN-H II composites. We use the X-ray data from *Chandra* to examine the nature of the ionizing sources in each system and measure the intrinsic X-ray luminosity for each nucleus. Our results provide the most statistically significant evidence for the elusive link between mergers and AGN in the X-rays. A large sample and a large dynamic range in merger separation are both crucial for discovering any subtle separation-dependent effects expected in the moderate AGN luminosity regime (e.g., Liu et al. 2012).

In addition, we present an X-ray census of (i) a parent sample of $\sim 10^4$ SDSS star-forming galaxies with close companions and (ii) a parent sample of $\sim 10^5$ SDSS single AGNs in isolated galaxies. These will be compared with the X-ray properties of optically selected AGN pair sample to put our results into context.

The paper is organized as follows. Section 2 describes our sample selection of the optical selected AGN pairs with archival X-ray observations and the construction of the comparison sample of star-forming galaxy pairs and the control sample of single AGNs in isolated galaxies. We present our method and analysis in Section 3 and the results in Section 4. Finally, we discuss the implications of our results in Section 5 and summarize in Section 6. Throughout this work, we quote errors at 68% confidence level unless otherwise noted.

2. SAMPLE SELECTION

2.1. *Optically Selected AGN Pairs with Archival Chandra Observations*

We start from the 1286 optically selected AGN pairs or multiples at a median redshift $\bar{z} \sim 0.1$ from Liu et al. (2011b). It was selected with projected separations $r_p < 100$ kpc and line-of-sight velocity offsets $\Delta v < 600$ km s⁻¹ from a parent sample of 138,070 AGNs spectroscopically identified based on their optical diagnostic emission-line ratios (i.e., the BPT diagram Baldwin et al. 1981; Veilleux & Osterbrock 1987; Kewley et al. 2001) and widths from the SDSS DR7 (Abazajian et al. 2009). We cross-matched this sample with the *Chandra* X-ray data archive for observations taken with the Advanced CCD Imaging Spectrometer (ACIS) which are publicly available as of May 2019. We requested both AGNs in a pair fall within 8' from the aimpoint and are covered by the ACIS field-of-view (FoV) to ensure both the observability and optimal angular resolution. We then visually checked all the matched targets, further excluding AGN pairs that fall on the ACIS-S4 CCD and a confirmed triple AGN (SDSS J0849+1114) recently discovered by Liu et al. 2019, see also Pfeifle et al. 2019a.

Our final sample consists of 67 AGN pairs with *Chandra* archival observations from the optically selected AGN pairs. Among them, 22 pairs are observed as the prime target. These include one triple AGN candidate optically identified by Liu et al. (2011a)² and five systems of AGN pairs studied by

¹ While the parent sample includes type 1, the parent sample is largely dominated by type 2 AGNs.

² The third nucleus of this candidate triple AGN J1027+1749 is not included in SDSS DR7, so we only count the separation between nuclei A and B.

Hou et al. (2019). The remaining 45 pairs were serendipitously observed. We address potential selection bias and incompleteness in §5.

2.2. Comparison and Control Samples

To put into context the X-ray detection rate of optically selected single/dual AGNs, we construct a comparison sample of star-forming galaxy (SFG) pairs from the SDSS legacy survey. These galaxy pairs are identified with the same criteria of projected separations $r_p < 100$ kpc and velocity offsets < 600 km s⁻¹, but are spectroscopically classified as H II nuclei using the BPT diagram. We have visually inspected all the pairs with small separations (< 5 – 10 kpc) to remove interlopers due to multiple fiber positions within the same galaxy with ~ 3000 SFG pairs left. We then cross-matched this parent list with the *Chandra* archive using the same criteria as for the AGN pairs. This resulted in a sample of 67 SFG pairs (the number is just coincidentally identical with the number of AGN pairs basically due to the non-survey nature of *Chandra* observations). There are only 2 SFG pairs with $r_p < 8$ kpc, in contrast to 15 AGN pairs with $r_p < 8$ kpc, which may be due in part to a selection bias (i.e., most close AGN pairs were covered by targeted *Chandra* observations).

To study the effects of merger-induced accretion, we also draw a control sample of 115 single AGNs in isolated galaxies with *Chandra* observations that are matched to each nucleus of the AGN pairs in redshift ($\Delta z \leq 0.004$) and stellar mass ($\log M_* \leq 0.05$). The isolated galaxies are defined as galaxies without any companion within a projected distance of 100 kpc. In cases where more than one matches are available for a given nucleus, we randomly pick one of them. The rest, $134 - 115 = 19$ nuclei in AGN pairs do not have matched single AGNs, either because their stellar mass is undetermined, or because the otherwise matched single AGNs have not been observed by *Chandra*.

Figure 1 shows the stellar mass and redshift distributions of the AGN pairs and those of the comparison and control samples. The AGN pairs have a median redshift $\bar{z} \sim 0.05$ and a median stellar mass $M_* \sim 4.9 \times 10^{10} M_\odot$. The control sample of single AGNs in isolated galaxies has similar redshift and stellar mass distributions, which ensures that any difference observed between the AGN pair and the single AGN samples will not be subject to redshift and/or mass-dependent biases. On the other hand, the comparison sample of SFG pairs, while also having a similar redshift distribution as the AGN pairs, has a systematically smaller stellar mass distribution. This may be partially due to an intrinsic difference between SFGs and the host galaxies of AGNs, because typical AGN host galaxies tend to be more massive than typical SFGs (e.g., Kauffmann et al. 2003).

3. METHOD AND ANALYSIS

3.1. *Chandra* Data Reduction

We reprocessed the archival *Chandra* data for all samples using CIAO v4.8 with the calibration files of CALDB v4.7.0 following standard procedures³. For targets with more than one observations that match our selection criteria, we adopted the one with the longest exposure. We examined the light curves and filtered time intervals of significant particle background. The effective exposure time of each target ranged from 1.8 ks to 123.1 ks. For each observation, we produced counts, exposure, and point-spread-function (PSF) maps on the original pixel scale ($0''.492$ pixel⁻¹) in the 0.5–2 (*S*), 2–8 (*H*), and 0.5–8 (*F*) keV bands. We have weighted the exposure maps by a fiducial incident spectrum, which is an absorbed power-law with a photon-index of 1.7 and an intrinsic absorption

³ <http://cxc.harvard.edu/ciao/>

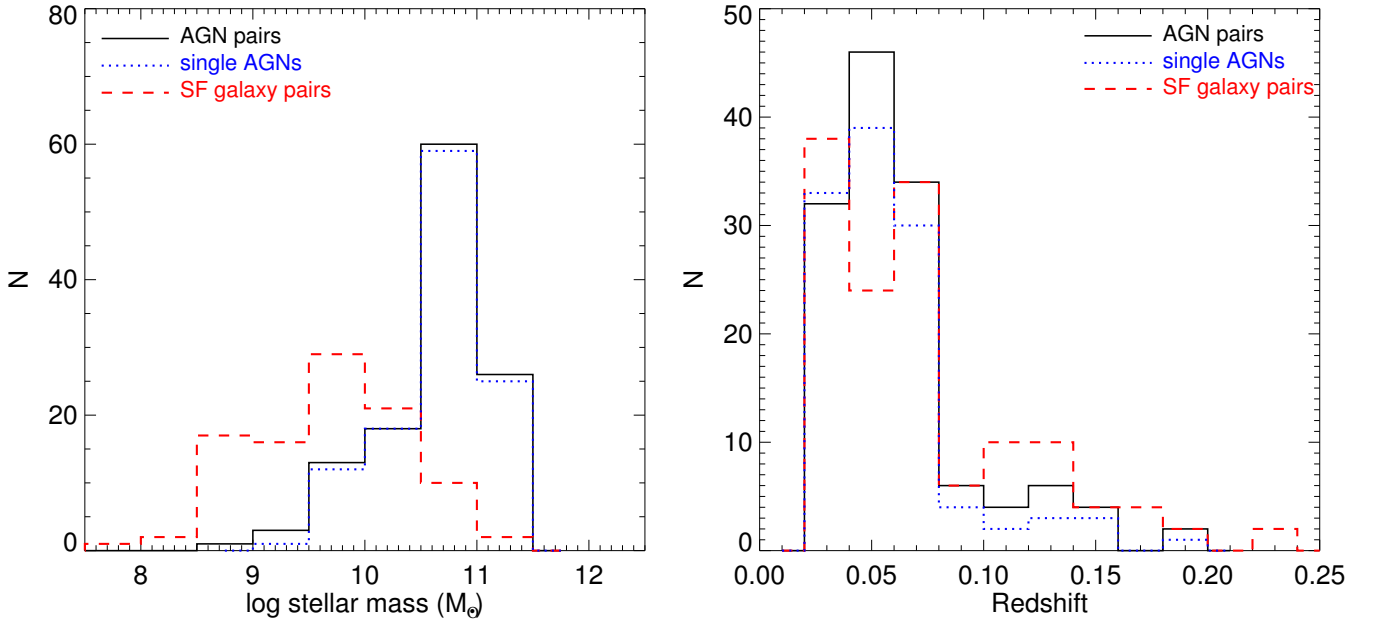


Figure 1. Stellar mass and redshift distributions of the AGN pairs and control samples of single AGNs and star-forming galaxy pairs, which are shown in black solid, red dashed and blue dotted histogram respectively.

column density $N_{\text{H}} = 10^{21} \text{ cm}^{-2}$. To ensure optimal sensitivity and accurate positioning for source detection, we have only used the data from the I0, I1, I2 and I3 CCDs for the ACIS-I observations and the S2 and S3 CCDs for the ACIS-S observations.

Table 1 lists the basic properties of AGN pairs. These include the SDSS name, celestial coordinates, redshift, projected separations r_p , stellar mass, total $[\text{O III}]$ flux (uncorrected for contribution from star formation), star formation rate estimates taken from the MPA-JHU DR7 catalog⁴, the *Chandra* observation ID, the *Chandra* instrument in use, and the effective X-ray exposure time.

3.2. X-ray Source Detection

We performed X-ray source detection in the 0.5–2, 2–8, and 0.5–8 keV bands for each observation using the CIAO tool *wavdetect*. We follow the method described in Hou et al. (2017) and Jin et al. (2019). We have supplied the exposure and 50% enclosed count fraction (ECF) PSF maps and have adopted a false detection probability of $P \leq 10^{-6}$. We have detected a total of 2223 independent X-ray sources in the *F* band, 1740 in the *S* band, and 1141 in the *H* band across the full field of view (FOV). We have also produced the sensitivity maps, which recorded the detection limit at each pixel (Kashyap et al. 2010). We have derived the detection limit at the position of each nucleus from the sensitivity maps.

Table 1 lists the *F* band detection limit of each target. It ranges between 5.2×10^{-7} and $8.7 \times 10^{-6} \text{ ph s}^{-1} \text{ cm}^{-2}$. Figure 2 shows the distributions of the detection limit for the three samples, which have been converted to the 0.5–8 keV intrinsic luminosity (see below for details). There is no significant difference in the detection limit among the three samples.

We use the CIAO tool *aprate* to calculate the net photon fluxes within the 90% enclosed count radius (ECR) for each detected point source in individual bands. In the few cases when two neighboring

⁴ <https://wwwmpa.mpa-garching.mpg.de/SDSS/DR7/>

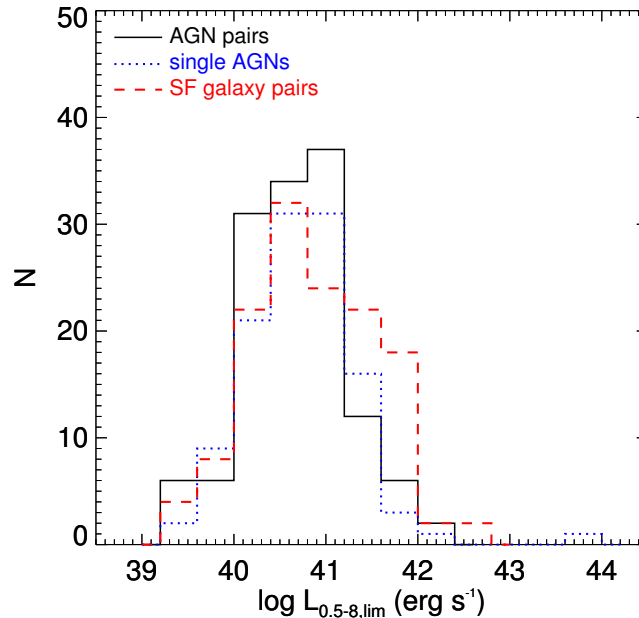


Figure 2. Distribution of the 0.5–8 keV (F band) luminosity detection limit of AGN pairs (black solid). Also shown are the control sample of single AGNs in isolated galaxies (blue dotted) and the comparison sample of star-forming galaxy pairs (red dashed).

sources have overlapping 90% ECR, we adopt a 50% ECR for photometry. We have subtracted the local background and have corrected for effective exposure and the ECF. The typical background region has been chosen to be between 2 to 5 times the 90% ECR with any detected X-ray sources removed in the region.

Assuming the incident power-law spectrum (i.e., with a photon-index of 1.7 and an intrinsic absorption column density $N_{\text{H}} = 10^{21} \text{ cm}^{-2}$), we have adopted a photon flux-to-intrinsic energy flux conversion factor of $2.2 \times 10^{-9} \text{ erg s}^{-1} \text{ cm}^{-2}/(\text{ph s}^{-1} \text{ cm}^{-2})$, $7.6 \times 10^{-9} \text{ erg s}^{-1} \text{ cm}^{-2}/(\text{ph s}^{-1} \text{ cm}^{-2})$, and $3.6 \times 10^{-9} \text{ erg s}^{-1} \text{ cm}^{-2}/(\text{ph s}^{-1} \text{ cm}^{-2})$ in the 0.5–2, 2–10, and 0.5–8 keV band. We have applied a K-correction appropriate for sources at different redshifts. To facilitate a direct comparison with previous studies, we have adopted a moderate extrapolation from the 2–8 keV to the 2–10 keV in the luminosity calculation. The assumed canonical absorption column density of 10^{21} cm^{-2} , while suitable for off-nuclear sources such as X-ray binaries, may be an underestimate for the nuclei if there is substantial intrinsic obscuration. The true 2–10 keV luminosity could be significantly higher than being reported here, but as we discuss below, this likely only affects a small fraction of the nuclei in our sample.

We adopt the same source detection procedures for the *Chandra* observations of the comparison and control samples. We have detected a total of 3960 independent sources in the F band, 3223 sources in the S band, and 2023 sources in the H band in the fields of single AGNs in isolated galaxies, and a total of 2147 independent sources in the F band, 1658 sources in the S band, and 1115 sources in the H band in the fields of SFG pairs. The majority of the detected sources may be due to the cosmic X-ray background or the Galactic foreground (e.g., Hou et al. 2017). A small fraction of the detected sources may also be associated with high-mass X-ray binaries possibly related to merger-induced star formation. We focus our discussion below on the detected nuclear X-ray sources and defer a detailed analysis of the off-nuclear sources to future work.

3.3. Identification of X-ray Counterparts

We search for X-ray counterparts of the AGN pairs from the list of detected sources using a matching radius of $2''$. This is chosen in view of the angular resolution of the SDSS imaging and the 90% ECR of *Chandra* in most cases. We have performed a random matching test by artificially shifting the positions of all nuclei by $\pm 10''$ in R.A. and Dec., which results in zero coincident match. As long as an optical nucleus is matched in any of the three energy bands, we consider it detected in the X-rays. For the nuclei that are not automatically picked up by *wavdetect*, we use the CIAO tool *aprate* to examine the $3\text{-}\sigma$ lower limit of X-ray flux at the optical nucleus position, following the procedures described in §3.2. If the flux lower limit is greater than zero, the source is regarded as an X-ray detection. From this procedure we have 12 additional nuclear X-ray sources detected in the *F* band, 11 sources in the *S* band, and 5 sources in the *H* band. For the non-detected nuclei, we derive the $3\text{-}\sigma$ flux upper limit using *aprate*. We have thus identified 74 nuclei with X-ray counterparts.

Visual inspection further identifies one additional nucleus, J122628.28+090126.4, whose SDSS fiber position deviates slightly from the true optical nucleus. A bright X-ray point source is found to be coincident with the nucleus and we include it as an X-ray-detected nucleus.

In summary, we have identified 75 nuclei with X-ray counterparts in total. Among them, 72 nuclei are detected in the *F* band, 69 nuclei in the *S* band, and 47 nuclei in the *H* band. Table 2 lists the net counts, 0.5–2 keV and 2–8 keV fluxes, and 0.5–2 keV and 2–10 keV intrinsic luminosities for the 75 X-ray-detected nuclei. In the few cases where the X-ray centroids of the nucleus differ significantly in different bands (e.g., the centroid may be problematic because of diffuse X-ray emission in the *S* band or low count levels in the *H* band), we take the *F* band centroid as the fiducial value and refine the photometry for the other bands. We have also identified X-ray nuclei in the control and comparison samples following the same procedure.

4. RESULTS

4.1. X-ray Detection Rates

Table 3 summarizes the X-ray detection rates. Among the sample of 67 optically selected AGN pairs with X-ray observations, 18 AGN pairs (i.e., $27\% \pm 6\%$) have both nuclei detected, 39 AGN pairs have only one of the two nuclei detected, and 10 AGN pairs have no X-ray detection. Figure 3 displays the SDSS optical *gri* color-composite images and the *Chandra* X-ray images of the 18 AGN pairs with both nuclei detected in the X-rays. We find an X-ray detection rate of $56\% \pm 6\%$ (75/134) among the 67 AGN pairs. In the subsample of AGN pairs with $r_p \gtrsim 10$ kpc, the X-ray detection rate is $47\% \pm 7\%$ (44/94). In the subsample of AGN pairs with $r_p \lesssim 10$ kpc, the X-ray detection rate is significantly larger, $78\% \pm 14\%$ (31/40). In the more conservative case where we only consider X-ray counterparts with $L_{2-10} > 10^{41}$ erg s $^{-1}$ as clearly detected AGNs (see discussion in §4.2), the X-ray detection rate becomes $27\% \pm 4\%$ (36/134) with 36 nuclei detected in the *H* band.

We find an X-ray detection rate of $57\% \pm 7\%$ (66/115) in the control sample of single AGNs in isolated galaxies. There are 60 nuclei detected in the *F* band, 58 nuclei in the *S* band, and 36 nuclei detected in the *H* band. This is consistent with the X-ray detection rate in AGN pairs within uncertainties. Our result suggests that the X-ray properties of optically selected AGN pairs are similar to those of optically selected single AGNs at least at $z \sim 0.1$.

On the other hand, we find a significantly lower X-ray detection rate of $17\% \pm 4\%$ (23/134) in the comparison sample of SFG pairs. There are 22 nuclei detected in the *F* band, 20 nuclei detected

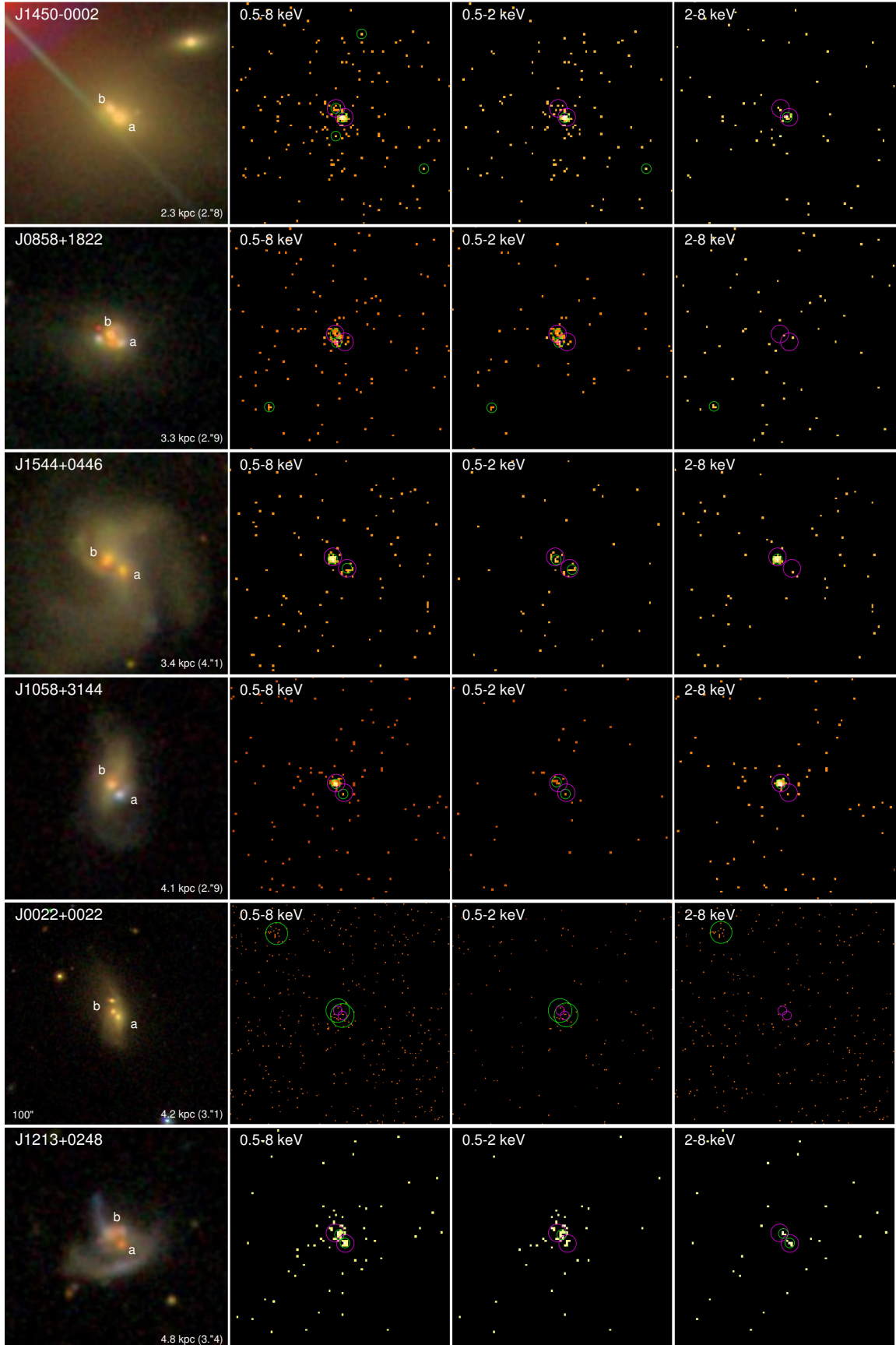


Figure 3. SDSS *gri*-color composite (first column), Chandra 0.5–8 keV (second column), 0.5–2 keV (third column), and 2–8 keV (last column) images of the 18 AGN pairs with both nuclei detected in the X-rays. Each panel is $50'' \times 50''$ unless otherwise labeled. North is up and east is to the left. The targets are ordered with increasing projected physical separation (as labeled, with angular distance in parenthesis). Magenta circles denote positions of the optical nuclei. Green circles represent the 90% ECR of the X-ray detections.

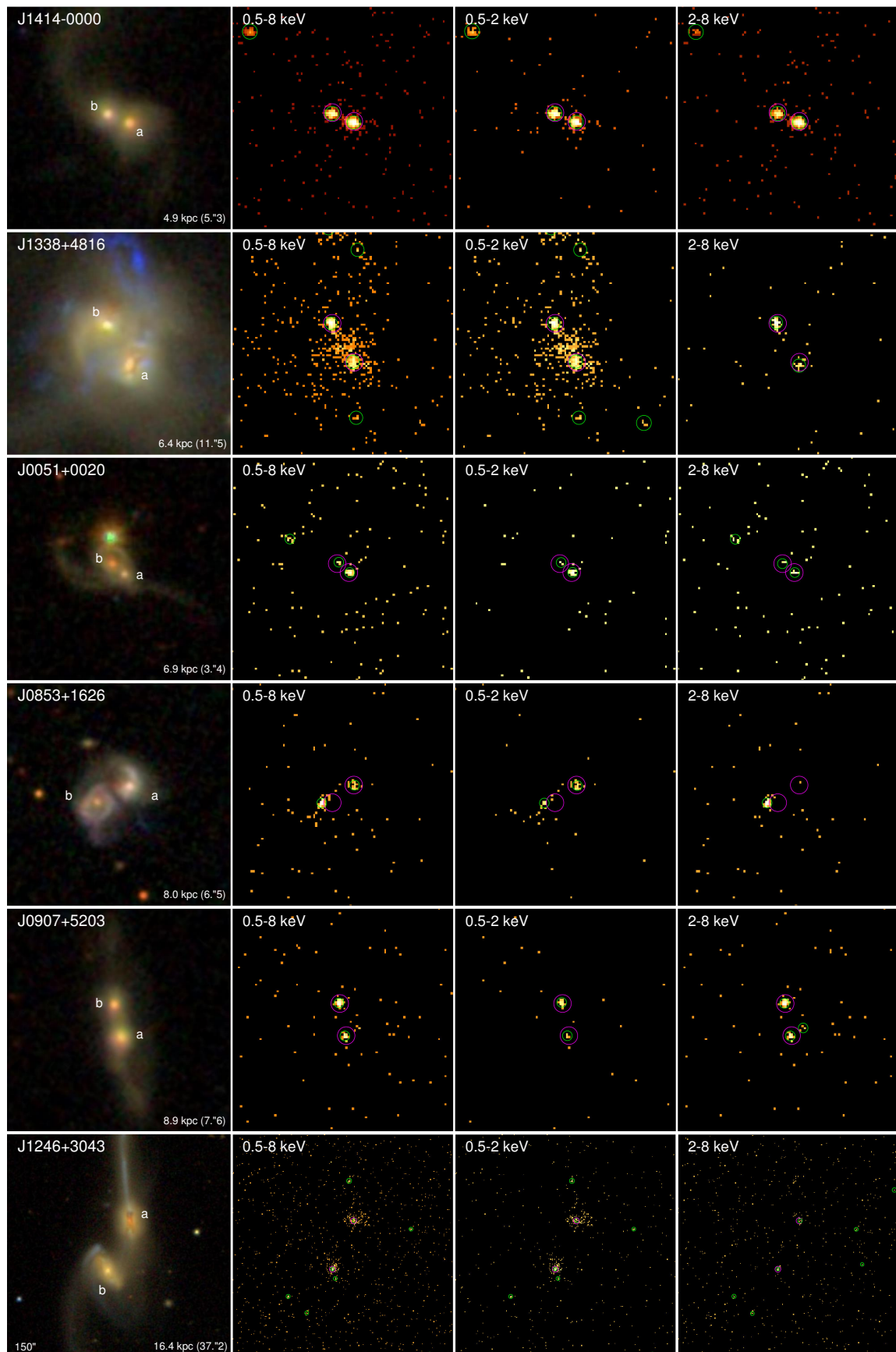


Figure 3. –continued

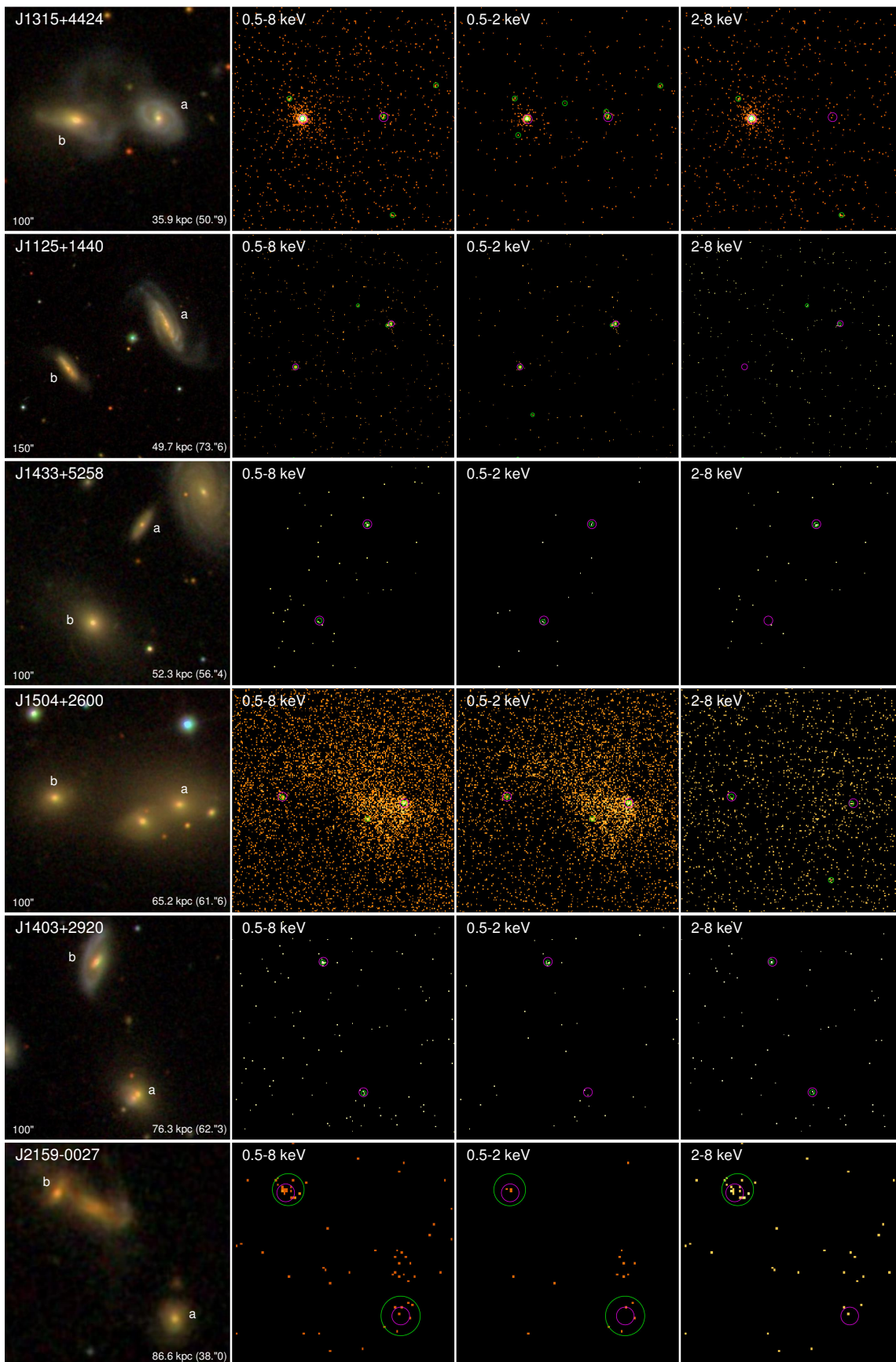


Figure 3. –continued

in the S band, and only 6 nuclei detected in the H band. There are 5 SFG pairs with both nuclei detected and 13 pairs with one nucleus detected. Figure 4 shows the optical and X-ray images of the 5 SFG pairs with both nuclei detected in X-rays. For the subsample of 78 nuclei among the SFG pairs with stellar masses $> 10^9 M_{\odot}$, which has a more similar stellar mass distribution to that of the AGN pairs, the X-ray detection rate is $21\% \pm 5\%$ (16/78). This is still much lower than that of the AGN pairs ($56\% \pm 6\%$, which is again $56\% \pm 7\%$, or 67/120, if we focus on AGN pairs with stellar masses $> 10^9 M_{\odot}$). This indicates that the X-ray emission from the AGN pairs has a minor contribution from star-formation-related processes. We address X-ray contamination from star-formation-related process further in §4.3.

The X-ray flux detection limit is highly inhomogeneous in our sample, which is primarily caused by the different exposure times of different systems (Table 2 and Figure 2). This may introduce selection biases into the resultant X-ray detections. For instance, we would have missed faint sources below the detection limit. We would also have been more likely to detect systems with targeted observations. To quantify this systematic, we examine the subsamples with an X-ray luminosity detection limit of $L_{0.5-8, \text{lim}} < 10^{41.2} \text{ erg s}^{-1}$. This threshold is chosen based on a two-sample Kolmogorov-Smirnov (K-S) test between the AGN pairs and the control and comparison samples. The significance level (probability of homogeneity) of the K-S statistic is 0.87 between AGN pairs and single AGNs and is 0.69 between AGN pairs and SFG pairs, respectively. This ensures a more homogeneous distribution between different samples and reduces the selection bias. These subsamples have 114 AGN pairs, 94 single AGNs, and 90 SFG pairs. Their X-ray detection rates are $57\% \pm 7\%$ (65/114), $63\% \pm 8\%$ (59/94), and $22\% \pm 5\%$ (20/90). The X-ray detection rate in the AGN pairs remains the same, while those in the single AGNs and SFG pairs increase slightly. Nevertheless, our conclusion on the comparison among different samples still holds. We discuss the implications of the X-ray detection rates in §5.

4.2. Global X-ray Properties

The left panel of Figure 5 shows the 2–10 keV intrinsic luminosity (L_{2-10}) against hardness ratio of all the X-ray-detected nuclei in the AGN pairs and the control and comparison samples. Table 1 lists the hardness ratio, which is defined as $\text{HR} = (H - S)/(H + S)$. It is calculated from the observed counts in the S (0.5–2 keV) and H (2–8 keV) bands using a Bayesian approach (Park et al. 2006). For sources that are not detected in the H band but are detected in the other two bands, we show the $3\text{-}\sigma$ upper limit of L_{2-10} in the plot. About forty sources, exclusively and about equally from the AGN pairs and single AGNs, are found at the top right portion with high luminosities ($L_{2-10} \gtrsim 10^{41.2} \text{ erg s}^{-1}$) and positive hardness ratios ($\text{HR} \gtrsim 0.1$); these are most likely genuine AGNs. Their hardness ratios suggest a moderately high absorption column density of $10^{22-23} \text{ cm}^{-2}$.

In contrast, a substantial fraction of sources are found at the bottom left portion with relatively low L_{2-10} (or H band non-detections) and negative HR; these include the majority of SFG pairs and a similar number of AGN pairs and single AGNs, indicating that the X-ray emission of these nuclei are more likely dominated by star formation activity rather than an AGN. However, it is still possible that some of these soft, under-luminous sources host an AGN in the center, but the hard X-ray emission is totally obscured due to a very high column density (i.e., Compton thick), leaving only circumnuclear soft X-ray emission falling within the *Chandra* aperture.

There are very few classical AGNs found among all the X-ray-detected nuclei, with all but four sources having $L_{2-10} > 10^{43} \text{ erg s}^{-1}$. This is further evidenced by the right panel of Figure 5, which

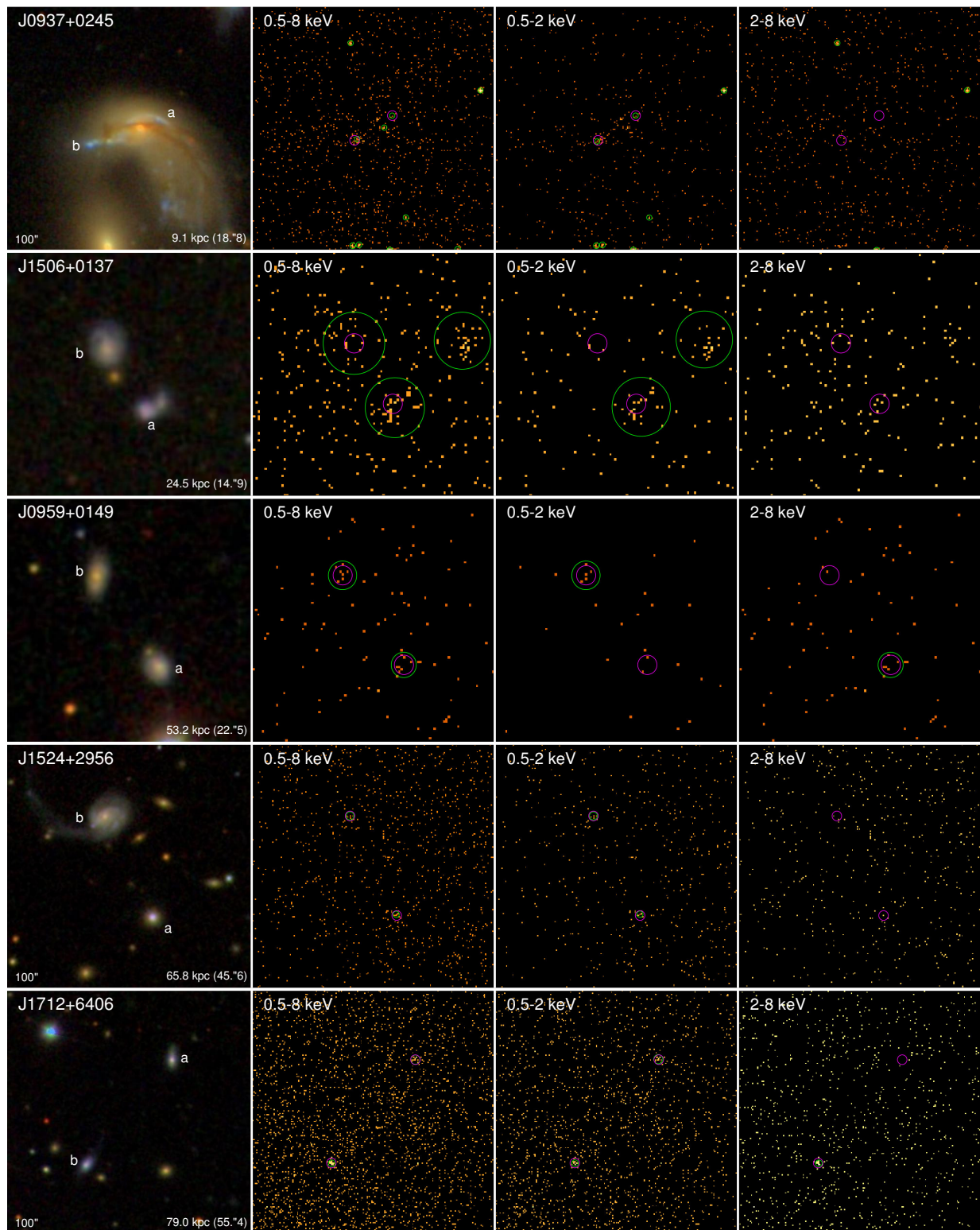


Figure 4. SDSS *gri*-color composite (first column), Chandra 0.5-8 keV (second column), 0.5-2 keV (third column), and 2-8 keV (last column) images of the 5 SFG pairs with both nuclei detected in X-ray. Each panel is $50'' \times 50''$ unless otherwise labeled. North is up and east is to the left. The targets are ordered with increasing projected separation (as labeled, with angular distance in parenthesis). Magenta circles denote positions of the optical nuclei whereas green circles represent the 90% ECR of the X-ray detections.

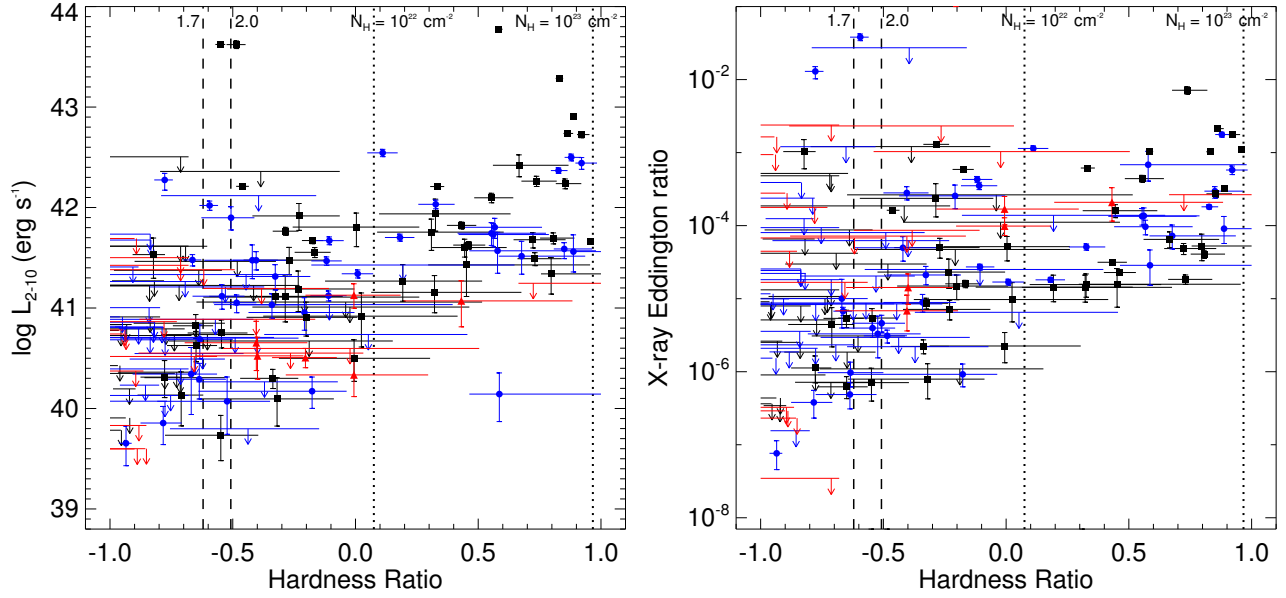


Figure 5. *Left:* 2–10 keV luminosity vs. hardness ratio. *Right:* X-ray Eddington ratio vs. hardness ratio. The black squares, blue circles and red triangles represent X-ray counterparts of AGN pairs, control samples of single AGNs and star-forming galaxy pairs, respectively. The vertical dashed lines, from left to right, correspond to hardness ratios for an absorbed power-law spectrum with a fixed $N_{\text{H}} = 10^{21} \text{ cm}^{-2}$ and a photon index of 2.0 and 1.7, respectively. The vertical dotted lines correspond to hardness ratios for an absorbed power-law spectrum with $N_{\text{H}} = 10^{22}, 10^{23} \text{ cm}^{-2}$ and a fixed photon index of 1.7.

plots the X-ray Eddington ratio against hardness ratio for sources that have a reliable estimate of the black hole mass (inferred from σ_* assuming the $M_{\text{BH}}\text{-}\sigma_*$ relation from Gültekin et al. 2009). Only four X-ray nuclei, one from AGN pairs and three from single AGNs, have an X-ray Eddington ratio of $\gtrsim 1\%$.

4.3. X-ray Contribution from Star Formation

Even in the absence of an AGN, circumnuclear star formation can produce copious X-ray emission, primarily attributed to high-mass X-ray binaries and diffuse hot gas heated by supernovae. We use independent SDSS spectroscopic star formation rates (SFR) given by the MPA-JHU DR7 catalog (listed in Table 1) to estimate the X-ray luminosity contributed from star formation. We adopt the empirical relation of Ranalli et al. (2003) given by,

$$L_{0.5-2}^{\text{SF}} = 4.5 \times 10^{39} \frac{\text{SFR}}{M_{\odot} \text{ yr}^{-1}} \text{erg s}^{-1}, \quad (1)$$

$$L_{2-10}^{\text{SF}} = 5.0 \times 10^{39} \frac{\text{SFR}}{M_{\odot} \text{ yr}^{-1}} \text{erg s}^{-1}, \quad (2)$$

which has an rms scatter of 0.27 dex and 0.29 dex in the 0.5–2 keV and 2–10 keV band, respectively.

Figure 6 shows the comparison between the measured X-ray luminosity and the empirical X-ray luminosity due to star formation in the two bands. The left panel shows that the majority of AGN pairs and single AGNs are located above the empirical relation, indicating that star formation contributes little to the observed 0.5–2 keV emission from these nuclei.

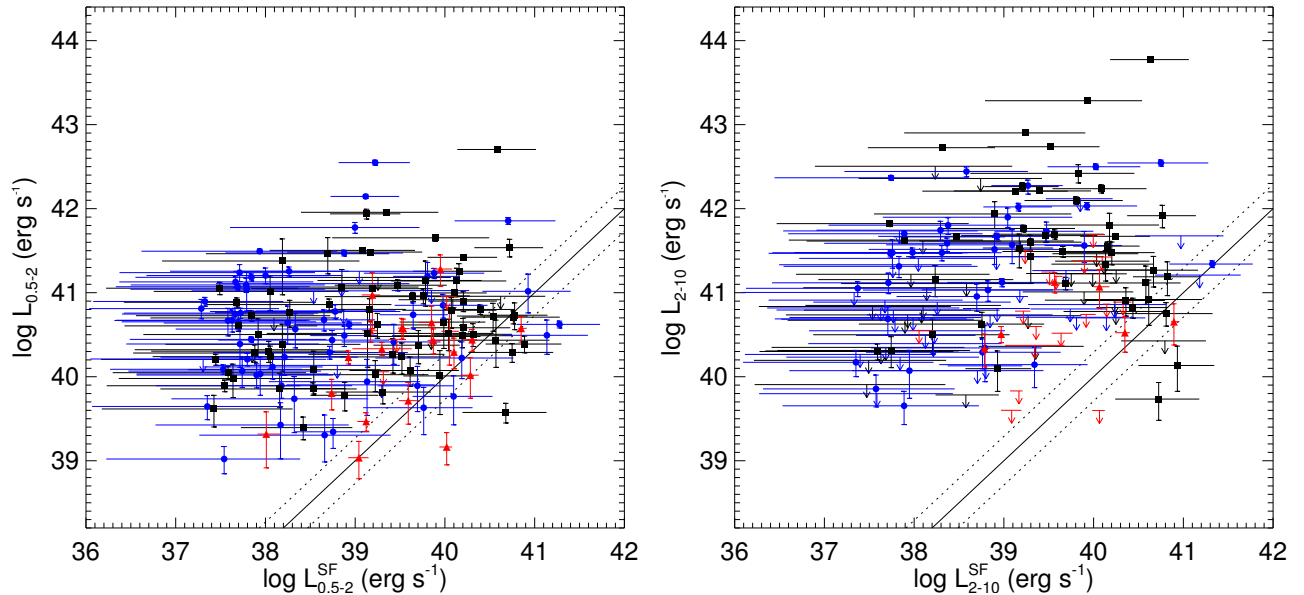


Figure 6. Measured 0.5–2 keV (*left*) and 2–10 keV (*right*) luminosity vs. predicted luminosity due to star formation. The black squares, blue circles and red triangles represent X-ray counterparts of AGN pairs, control samples of single AGNs and star-forming galaxy pairs, respectively. The black solid line indicates a 1:1 relation, with the pair of dashed lines representing the rms scatter.

However, there is still a significant fraction of AGN pairs overlapping with the SFG pairs, with a notable fraction of the latter sitting above the empirical relation. This may suggest either an underestimate of star formation contribution by the calibration of [Ranalli et al. \(2003\)](#) (e.g., due to a redshift-dependent effect), or the presence of an optically hidden AGN that moderately contributes to the soft X-ray emission.

The right panel shows that the predicted contribution from star formation for almost all AGN pairs (as well as single AGNs) is well below the measured 2–10 keV luminosity. The SFG pairs are well separated from the AGN pairs, with only few SFG pairs firmly detected in this band. We have also compared the prediction of [Ranalli et al. \(2003\)](#) with the empirical correlation between 2–10 keV luminosity $L_{\text{HX}}^{\text{gal}}$, SFR, and stellar mass from [Lehmer et al. \(2010\)](#), given by

$$L_{\text{HX}}^{\text{gal}} = \alpha M_* + \beta \text{SFR}, \quad (3)$$

where $\alpha = (9.05 \pm 0.37) \times 10^{28} \text{ erg s}^{-1} M_{\odot}^{-1}$ and $\beta = (1.62 \pm 0.22) \times 10^{39} \text{ erg s}^{-1} (M_{\odot} \text{ yr}^{-1})^{-1}$. The calibration was based on a sample of 17 LIRGs. The X-ray emission includes both the contribution from high-mass X-ray binaries and low-mass X-ray binaries. The predicted 2–10 keV luminosities are consistent within uncertainties between AGN pairs and SFG pairs. This suggests that the 2–10 keV emission of AGN pairs (as well as single AGNs) is dominated by genuine AGN activity. Single AGNs tend to have a lower SFR than the AGN pairs, which may indicate that the X-ray emission from single AGNs are even less effected by star formation.

In view of the above, we consider X-ray nuclei with $L_{2-10} > 10^{41} \text{ erg s}^{-1}$ as genuine AGNs. In this more conservative case, the X-ray detection rate is $27\% \pm 4\%$ for AGN pairs, $23\% \pm 5\%$ for single AGNs, and $1\% \pm 1\%$ for SFG pairs (Table 3). Below we focus our discussion on the 2–10 keV band.

4.4. Comparison with $[O \text{ III}]$ Luminosity

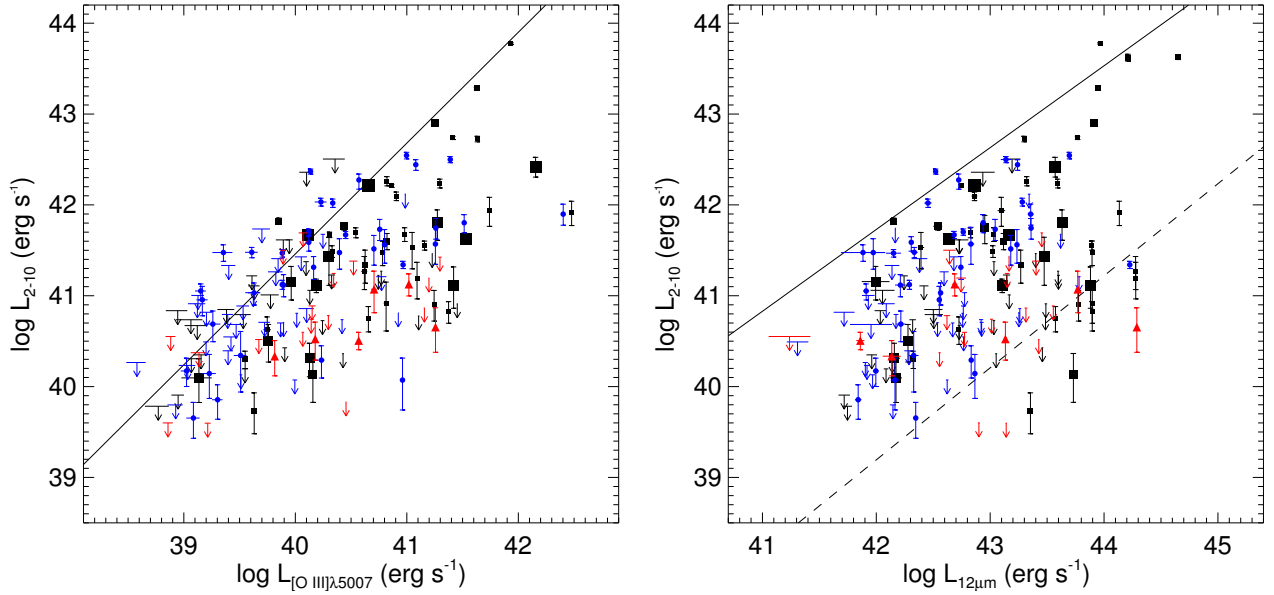


Figure 7. *Left:* Measured 2–10 keV luminosity vs. extinction-corrected [O III] luminosity. The black solid line indicates the mean relation for optically selected Type 1 and Type 2 Seyferts (Panessa et al. 2006). *Right:* Measured 2–10 keV luminosity vs. mid-infrared 12 μ m luminosity. The black solid line indicates the mean relation for local Seyferts (Gandhi et al. 2009), while the dashed line is a predicted relation between the two quantities if both are related to star formation (see text). In both panels, the black squares, blue circles and red triangles represent X-ray counterparts of AGN pairs, control samples of single AGNs and star-forming galaxy pairs, respectively. The size of the black squares is linearly proportional to the projected separation (r_p) of the pair in which a given AGN resides.

The left panel of Figure 7 shows the 2–10 keV luminosity against the extinction-corrected [O III] luminosity. The extinction of [O III] luminosities has been corrected according to the observed Balmer decrement. The [O III] luminosity is an empirical AGN indicator, which is related to the 2–10 keV X-ray luminosity as (Panessa et al. 2006),

$$\log L_{2-10\text{keV}} = (1.22 \pm 0.06) \log L_{[\text{O III}]} + (-7.34 \pm 2.53). \quad (4)$$

The relation was calibrated based on both optically-selected Type 1 and Type 2 Seyferts after extinction correction. Objects in our sample of single AGNs are consistent with the empirical relation at least over the range of $10^{39} \text{ erg s}^{-1} \lesssim L_{[\text{O III}]} \lesssim 10^{41} \text{ erg s}^{-1}$, where the majority of single AGNs are found. On the other hand, the AGN pairs on average lie below the empirical relation, which indicates a systematically smaller X-ray-to-[O III] luminosity ratio in AGN pairs than in single AGNs in isolated galaxies.

Previous work based on smaller samples has found evidence for a systematically smaller hard-X-ray-to-[O III] luminosity ratio in optically selected dual AGNs than in single AGNs (e.g., Liu et al. 2013; Hou et al. 2019). With a much larger sample of AGN pairs, we here confirm the X-ray weak tendency in optically selected AGN pairs. This puts the result on firmer statistical ground. Moreover, among the ~ 60 nuclei in AGN pairs found below the empirical line, roughly half have $r_p \lesssim 10$ kpc and half have $r_p \gtrsim 10$ kpc. Finally, the SFG pairs are almost exclusively located below the AGN relation, which is consistent with the picture where star-formation-related processes produce systematically weaker X-ray emission at a given [O III] luminosity.

4.5. Comparison with Mid-Infrared Luminosity

The right panel of Figure 7 compares the 2–10 keV luminosity with the mid-infrared (MIR) 12 μm luminosity. The 12 μm luminosity was derived from the *WISE* survey (Wright et al. 2010). Shown for context is an empirical relation (the solid line) between the X-ray and MIR luminosities of a sample of local Syferts of both Type 1 and Type 2 (Gandhi et al. 2009) given by,

$$\log(L_{12\mu\text{m}}/10^{43} \text{ erg s}^{-1}) = (0.19 \pm 0.05) + (1.11 \pm 0.07) \log(L_{2-10}/10^{43} \text{ erg s}^{-1}). \quad (5)$$

The MIR emission is thought to arise from the torus reprocessing the AGN radiation.

Nearly all AGN pairs fall below the empirical relation found in single AGNs by up to ~ 2 dex for a given 12 μm luminosity. This appears to suggest that our 2–10 keV luminosity is significantly underestimated, e.g., due to strong obscuration caused by a merger-driven gas concentration effect. However, we argue that this is unlikely for two reasons. First, the observed X-ray hardness ratio suggests that only a small number of nuclei in AGN pairs have an absorption column density close to 10^{23} cm^{-2} (Figure 5), at which level the 2–10 keV luminosity would only be decreased by ~ 0.4 dex (e.g., Satyapal et al. 2017). Second, there is no systematic difference between the X-ray harness ratio distributions of AGN pairs and single AGNs, which indicates no systematic excess in the X-ray obscuration in AGN pairs relative to single AGNs.

A more plausible explanation is an excess MIR luminosity due to contamination by the host galaxy, since the WISE aperture (FWHM $6'' - 12''$) is significantly larger than the *Chandra* PSF. This is supported by the fact that the SFG pairs have similar 12 μm luminosities to those seen in the AGN pairs. For instance, a typical SFR of $10 M_{\odot} \text{ yr}^{-1}$ can account for a 12 μm luminosity of $10^{43.5} \text{ erg s}^{-1}$, according to the $L_{12\mu\text{m}}$ -SFR relation of Donoso et al. (2012),

$$\log(L_{12\mu\text{m}}^{\text{SF}}/\text{erg s}^{-1}) = 0.987 \log(\text{SFR}/M_{\odot} \text{ yr}^{-1}) + 42.5. \quad (6)$$

This can be further translated into a $L_{2-10}^{\text{SF}} - L_{12\mu\text{m}}^{\text{SF}}$ relation assuming that both luminosities are due to star formation (Gross et al. 2019), which is shown by the dashed line in the right panel of Figure 7. Those AGN pairs with $L_{2-10} \lesssim 10^{41} \text{ erg s}^{-1}$ may suffer from an overestimation of the AGN MIR luminosity due to contamination from star formation.

4.6. AGN X-ray Luminosity versus Projected Separation

The sizable sample of AGN pairs allows us, for the first time from an X-ray perspective, to examine the causal link between AGN activity and pair separation, which has been suggested by simulations of galaxy merger (e.g., Rosas-Guevara et al. 2019). The projected pair separation is used as a proxy for the merger phase, where larger (smaller) r_p represents the earlier (later) stage of a merger.

Figure 8 shows the 2–10 keV luminosity or upper limits for non-detected sources as a function of projected separations r_p for AGN pairs and the comparison sample of SFG pairs. Perhaps the most surprising finding is the paucity of X-ray luminous nuclei at small separations ($r_p \lesssim 4 \text{ kpc}$). Moreover, a clear trend is revealed when we bin the AGN pairs by their separations to reduce the scatter in the mean. The mean X-ray 2–10 keV luminosity of each r_p -bin is calculated using Astronomy SURVival Analysis (ASURV; Feigelson & Nelson 1985), which takes both detections and upper limits into account. For targets with $r_p \lesssim 20 \text{ kpc}$, the mean X-ray 2–10 keV luminosity declines as r_p decreases. This trend is the opposite to that seen in the $[\text{O III}]$ luminosity versus r_p relation in AGN pairs (Liu et al. 2012, see also below) and that seen in single AGNs in galaxy pairs (e.g., Ellison et al. 2011).

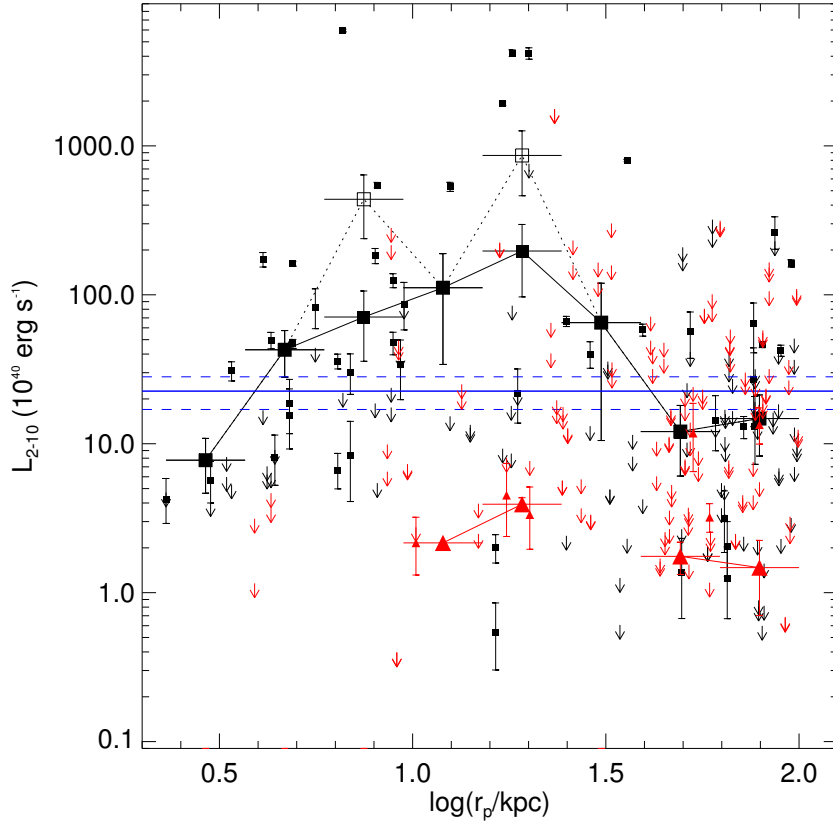


Figure 8. X-ray 2–10 keV luminosity as a function of projected physical separations r_p . The X-ray detected AGN pairs and star-forming galaxy pairs are shown in smaller black squares and red triangles, respectively. The $3\text{-}\sigma$ upper limit of undetected nuclei are shown in arrows. For each r_p bin, the mean luminosities of AGN pairs and star-forming galaxy pairs are shown in larger black squares and red triangles with 1σ error bars connected by line, respectively. Two larger open black squares at the third and fifth r_p bins of AGN pairs include all the sources while the larger solid black squares exclude the three most luminous nuclei. In a few bins the mean luminosity of star-forming galaxy pairs is undetermined due to the lack of firm detections in these bins. The blue horizontal solid line shows the mean value of 2–10 keV luminosity of single AGNs, and the dashed blue lines represent the $\pm 1\sigma$ error bars.

The mean X-ray 2–10 keV luminosity of the innermost bin ($r_p \lesssim 4$ kpc) is significantly lower than the mean luminosity averaged over all single AGNs (also calculated with ASURV; represented by the blue lines in Figure 8). The mean X-ray luminosity also decreases as r_p increases from ~ 20 kpc beyond until about 100 kpc, which is the largest separation spanned by our samples. We should note that in calculating the mean luminosities in Figure 8, we have excluded the three most luminous nuclei ($> 3 \times 10^{43}$ erg s^{-1}), because they seem to be outliers. But the overall trend remains qualitatively unchanged if these three nuclei were included.

We have tested systematic effects the inhomogeneous detection limits by including only those pairs with a detection limit of $L_{0.5-8,\text{lim}} < 10^{41.2}$ erg s^{-1} (see also §4.1). The overall trend stays unaffected using this homogeneous detection limit.

For the SFG pairs, due to the lack of X-ray detected nuclei (6 sources) particularly at $r_p \lesssim 4$ kpc, we only have four bins with available mean 2–10 keV luminosities. Nevertheless, the trend in the

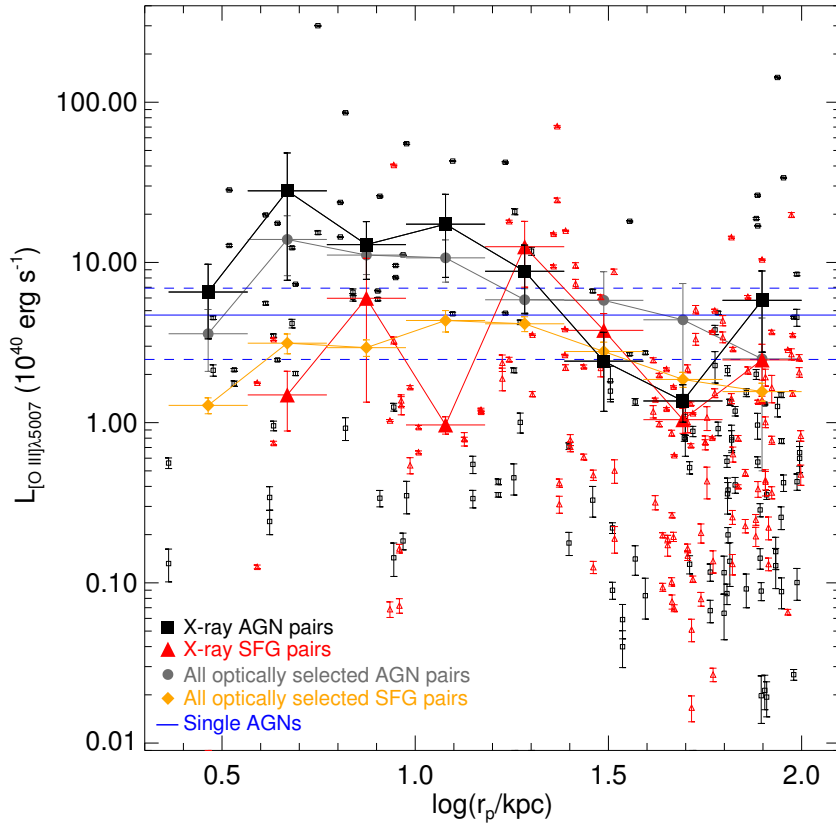


Figure 9. $[\text{O III}]$ luminosity as a function of projected separations r_p . All AGN pairs and star-forming galaxy pairs with *Chandra* observation are shown in smaller open black squares and red triangles, respectively. For each r_p bin, the mean luminosities of AGN pairs and star-forming galaxy pairs are shown in larger solid black squares and red triangles connected by line, respectively. We also show the mean luminosities of all optically selected AGN pairs in gray solid circles and the mean luminosities of all optically selected star-forming galaxy pairs in orange solid diamonds. The blue horizontal solid line shows the mean value of $[\text{O III}]$ luminosity of single AGNs.

SFG pair sample is still generally flat. The mean X-ray 2–10 keV luminosities are much lower than those in both AGN pairs and single AGNs.

Figure 9 shows the mean $[\text{O III}]$ luminosity as a function of projected separation r_p . We use the mean value to be consistent with the above analysis of the X-ray luminosity. For all AGN pairs with *Chandra* observation, the mean $[\text{O III}]$ luminosity increases with decreasing separation. This increasing trend extends until the innermost bin at $r_p \sim 4$ kpc, which is much more inward than that seen in the X-ray luminosity. The separation dependence flattens out at large r_p ($\gtrsim 30$ kpc). There was no declining trend in the innermost bin in a similar plot of Liu et al. (2012). There are two possible reasons for this difference. First, the $[\text{O III}]$ luminosity quoted in Liu et al. (2012) has been corrected for contribution from star formation following the procedure of Kauffmann & Heckman (2009). Second, we quote mean values here whereas median values were quoted in Liu et al. (2012) and the difference may be due to small number statistics. The innermost bin is highly incomplete due to the angular resolution limit of SDSS imaging ($\sim 2''$ corresponding to ~ 4 kpc at redshift $z \sim 0.1$).

4.7. Three Newly Discovered X-ray Dual AGN Systems

Our X-ray survey has uncovered three new dual AGN systems whose X-ray properties have not been reported in the literature. Below we discuss these systems in detail. 4 lists their physical measurements.

SDSS J1450–0002 The separation of this AGN pair is 2.3 kpc as shown in Figure 3. Both galaxies in the merger are optically classified as H II/AGN composites or LINERs. The SW nucleus (J1450-0002a) is detected in both the *S* and *H* bands, whereas the NE nucleus (J1450-0002b) is detected in the *F* band only. For the SW nucleus, the comparison between the observed to the expected star-formation-induced X-ray luminosities (Table 4) are consistent with the AGN scenario. For the NE nucleus, on the other hand, the upper limits of the X-ray luminosity in the *S* and *H* bands are still consistent with the presence of an additional AGN, although the possibility that one AGN in the NW nucleus ionizes gas in both galaxies cannot be ruled out.

SDSS J0858+1822 This is a candidate triple AGN system. But the third nucleus is not included in SDSS DR7. The separation (3.3 kpc) of this system is calculated between nuclei A and B as shown in Figure 3. The NE nucleus (J0858+1822b) in the merger is optically classified as a Type 2 Seyfert whereas the SW nucleus (J0858+1822a) a Type 2 Seyfert or a LINER. Both NE and SW nuclei are detected in the *S* band only. However, the X-ray counterpart of SW nucleus looks more likely correlated to a third nucleus between pairs. For both nuclei, the observed X-ray luminosities are similar to those expected from star formation-induced X-ray luminosities (Table 4), although an additional AGN component cannot be ruled out given significant uncertainties in the estimate.

SDSS J1414–0000 The separation of this AGN pair is 4.9 kpc as shown in Figure 3. The SW nucleus (J1414-0000a) in the merger is optically classified as a Type 2 Seyfert whereas the NE nucleus (J1414-0000b) a H II/AGN composite. Both nuclei are detected in both the *S* and *H* bands and are luminous. For both nuclei, the expected star-formation-induced X-ray luminosities are too low to explain the observed values in both the *S* and *H* bands (Table 4), consistent with the AGN scenario.

5. DISCUSSION

The current work represents the first to study the effects of mergers in optically selected AGN pairs from an X-ray perspective in a statistically meaningful sense. Previous studies based on the parent sample of optically-selected AGN pairs has found evidence for tidally enhanced AGN in both AGN pairs (e.g., Liu et al. 2012) and in single AGNs in galaxy pairs (e.g., Ellison et al. 2011). These studies, however, have adopted the [O III] luminosity as an indicator for AGN luminosity. As discussed in §1, the X-ray band provides not only an independent but also a more direct and robust diagnostic of AGN. This is especially helpful for the regime of low luminosity/low Eddington ratio characteristic of the current sample, where the casual link between mergers and AGN has been controversial and more difficult to probe due to the competition of secular processes (e.g., Liu et al. 2012).

Our X-ray census enriches this picture in two aspects. First, the X-ray detection rate in AGN pairs is substantially higher than that in SFG pairs, which holds true for the whole sample as well as several sub-samples constructed to test various systematics (§4.1 and Table 3). In the more conservative case where a genuine AGN is required to have an X-ray 2–10 keV luminosity greater than 10^{41} erg s⁻¹, the detection rate is $\sim 27\%$. The X-ray detection rate provides a useful constraint for the triggering of AGN pairs, which is the subject of several recent theoretical studies (Capelo et al. 2017; Rosas-Guevara et al. 2019; Solanes et al. 2019; Yang et al. 2019a). For instance, using a suite of major merge simulations, Solanes et al. (2019) predicted an abundance of 5% – 30% weakly accreting AGN pairs (i.e., with bolometric luminosities $\lesssim 10^{43}$ erg s⁻¹) under an observational condition tailored

to match the selection criteria of our parent sample (Liu et al. 2011b). While current simulations generally cannot self-consistently predict the accretion-induced X-ray luminosity, our X-ray detection rates appear to be broadly consistent with predictions from simulations.

Second, the X-ray detection rate is statistically indistinguishable between the samples of AGN pairs and single AGNs in isolated galaxies. Moreover, the samples of single AGNs and AGN pairs span a similar range in X-ray luminosity and Eddington ratio (Figure 5). This underscores the challenge in distinguishing the roles of galaxy-galaxy interaction and internal, secular processes in triggering and maintaining a moderate level of SMBH accretion. Our result is consistent with the picture where the overall weak enhancement in AGN luminosity/Eddington ratio observed in optically-selected close AGN pairs represents enhanced BH accretion on top of a background of low-level AGN driven by secular processes not directly associated with galaxy interactions (Liu et al. 2012).

Nevertheless, the mean 2–10 keV luminosity as a function of projected separation shown in Figure 8 does suggest that galaxy-galaxy interactions do affect the X-ray emission. The increase in the X-ray luminosity as r_p decreases from $r_p \gtrsim 50$ kpc to $r_p \sim 20$ kpc may be evidence for enhanced SMBH accretion at the first pericentric passage at the early stage of a merger, consistent with predictions from simulations (e.g., Rosas-Guevara et al. 2019). The decrease of the X-ray luminosity from $r_p \sim 15$ kpc inward, however, is rather surprising. This appears to be contradictory to expectations from simulations, where tidal torques would funnel more gas into the center to drive stronger SMBH accretion as observed in [O III] luminosity (e.g., Liu et al. 2012).

In addition to small number statistics, there are at least two other possibilities to explain the decrease of X-ray luminosity at the smallest separations. First, merger-induced gas inflows could become so strong that a central concentration of cold gas heavily obscures even the hard (2–10 keV) X-rays. Indeed, there is growing evidence for heavily obscured close AGN pairs on kpc-scales (e.g., Satyapal et al. 2017; Pfeifle et al. 2019b). The systematically lower X-ray-to-[O III] luminosity ratio in the AGN pairs (§4.4) may also be a merger-driven gas concentration effect. This would preferentially obscure the X-rays which originate from regions closer to the SMBH than the [O III] emission. However, a low X-ray-to-[O III] luminosity ratio is found in AGN pairs of both small and large separations. Therefore, other factors such as a selection bias in the [O III] luminosity cannot be completely ruled out (e.g., Liu et al. 2013).

Second, AGN feedback triggered by the first pericentric passage could act to heat and expel gas from the central region and suppress subsequent SMBH accretion. Our results may be compared with merger simulations incorporating the effect of AGN feedback. The effect of feedback in AGN pairs can in principle be tested using direct tracers such as the circumnuclear diffuse hot gas and/or outflows of ionized gas. In fact, in an appreciable fraction of AGN pairs studied here, we find clear evidence for the presence of circumnuclear diffuse X-ray emission (such as in J1213+0248, J1338+4816 (i.e., Mrk266), J0853+1626, J1504+2600, etc. in Figure 3), , which may be related to AGN feedback. We defer a systematic study of diffuse X-ray emission around AGN pairs to future work.

Finally, we discuss the caveats and limitations of our results. While representing the currently largest sample of X-ray-detected AGN pairs matched from an optically selected sample, it is still subject to small number statistics. Future X-ray observations with much larger samples are needed to put our results on firmer statistical ground. The current sample is also strongly biased toward AGN pairs with close separations (20 of the 67 pairs have $r_p \lesssim 10$ kpc), due to the fact that essentially all targeted *Chandra* observations were for close pairs. Only $\sim 70\%$ of our archival sample were observed

by chance and would be free from a selection bias. Fortunately, this selection bias toward small r_p actually helps reveal the paucity of X-ray-luminous nuclei in close pairs. A complete study of the effects of merger-driven AGN must also include interacting galaxy pairs at large separations ($10 \text{ kpc} \lesssim r_p \lesssim 100 \text{ kpc}$), which should be more favorably targeted by future observations.

In zoom-in merger simulations, a galaxy pair would evolve in isolation, i.e., free from perturbation by a third galaxy, which is not necessarily the case in the observations. The comparison may be improved by carefully choosing truly isolated galaxy pairs for future observations (e.g., [Argudo-Fernández et al. 2015](#)). Another mismatch between the current *Chandra* sample and merger simulations is the fraction of major mergers (usually defined as those having a primary-to-secondary stellar mass ratio ≤ 3), which is $\sim 50\%$ in the observations. More simulation work is needed to study the triggering of AGN activity in minor mergers (e.g., [Yang et al. 2019b](#)).

6. SUMMARY

We have presented the first systematic X-ray study of optically selected AGN pairs in a statistical sample ($> 10^2$) at redshift $z \sim 0.1$. We have performed X-ray matches and detections with the *Chandra* data archive for a parent sample of [O III]-selected AGN pairs, a comparison sample of star-forming galaxy pairs, and a carefully drawn control sample of single AGNs in isolated galaxies. We summarize our main findings as follows:

1. We have detected at least one compact X-ray nuclei in 57 out of the 67 optically selected AGN pairs. The X-ray detection of both nuclei has confirmed AGN pairs in 18 optically selected systems, including 3 new discoveries of dual AGNs (i.e., AGN pairs with projected separations $< 10 \text{ kpc}$). The detection rate of X-ray nuclei is significantly higher in AGN pairs than in the comparison sample of star-forming galaxy pairs.
2. We have measured the X-ray 2–10 keV luminosity for the detected X-ray nuclei based on the observed X-ray counts assuming a canonical power-law spectrum. The X-ray 2–10 keV luminosity of most AGN pairs (ranging between $5.4 \times 10^{39} - 6.0 \times 10^{43} \text{ erg s}^{-1}$) also substantially exceeds the empirically predicted luminosity by star formation. Our results suggest that a large fraction of the X-ray-detected nuclei are genuine AGNs, lending support to their optical identification.
3. We have studied the X-ray 2–10 keV luminosity of optically selected AGN pairs as a function of projected pair separation (r_p). The X-ray 2–10 keV luminosity increases as r_p decreases from $\gtrsim 50 \text{ kpc}$ to $\sim 15 \text{ kpc}$. However, it decreases with further decreasing r_p at $r_p < 15 \text{ kpc}$, in contrast to theoretical predictions from merger simulations and to the empirical trend previously seen in [O III] luminosity. The apparent scarcity of X-ray luminous nuclei at r_p smaller than a few kpc may be caused by heavy obscuration induced by merge-driven gas inflows. Alternatively, this may result from a negative feedback from merger-driven AGNs that already happens at the first pericentric passage and suppresses further black hole accretion or small number statistics.

Our results contribute to the understanding of the accretion and demographics of SMBHs in merging galaxies and the effects of merger-induced AGN on galaxy evolution. The X-ray confirmation of a statistical sample of dual AGNs is only enabled by the synergy between *Chandra* and SDSS, constituting an indispensable legacy for further more detailed studies. A continued effort of identifying

such systems in larger numbers and characterizing their fundamental properties systematically in the X-rays will be highly rewarding.

ACKNOWLEDGEMENTS

M.H. and Z.L. acknowledge support by the National Key Research and Development Program of China (2017YFA0402703). X.L. acknowledges support by NASA through Chandra Award Number GO3-14104X issued by the Chandra X-ray Observatory Center, which is operated by the Smithsonian Astrophysical Observatory for and on behalf of NASA under contract NAS 8-03060. We thank Yanmei Chen, Paul Green, Ralph Kraft and Jianfeng Wu for useful discussions, and Yali Zhu for help with the *Chandra* data preparation at the early stage of this work.

This research has made use of software provided by the *Chandra* X-ray Center in the application packages CIAO, ChIPS, and Sherpa.

Funding for the Sloan Digital Sky Survey IV has been provided by the Alfred P. Sloan Foundation, the U.S. Department of Energy Office of Science, and the Participating Institutions. SDSS-IV acknowledges support and resources from the Center for High-Performance Computing at the University of Utah. The SDSS web site is www.sdss.org.

SDSS-IV is managed by the Astrophysical Research Consortium for the Participating Institutions of the SDSS Collaboration including the Brazilian Participation Group, the Carnegie Institution for Science, Carnegie Mellon University, the Chilean Participation Group, the French Participation Group, Harvard-Smithsonian Center for Astrophysics, Instituto de Astrofísica de Canarias, The Johns Hopkins University, Kavli Institute for the Physics and Mathematics of the Universe (IPMU) / University of Tokyo, Lawrence Berkeley National Laboratory, Leibniz Institut für Astrophysik Potsdam (AIP), Max-Planck-Institut für Astronomie (MPIA Heidelberg), Max-Planck-Institut für Astrophysik (MPA Garching), Max-Planck-Institut für Extraterrestrische Physik (MPE), National Astronomical Observatories of China, New Mexico State University, New York University, University of Notre Dame, Observatório Nacional / MCTI, The Ohio State University, Pennsylvania State University, Shanghai Astronomical Observatory, United Kingdom Participation Group, Universidad Nacional Autónoma de México, University of Arizona, University of Colorado Boulder, University of Oxford, University of Portsmouth, University of Utah, University of Virginia, University of Washington, University of Wisconsin, Vanderbilt University, and Yale University.

Facilities: *Chandra* X-ray Observatory (ACIS), Sloan

Software: CIAO (Fruscione et al. 2006), Sherpa (Freeman et al. 2001; Doe et al. 2007), ChiPS (Germain et al. 2006)

REFERENCES

- Abazajian, K. N., Adelman-McCarthy, J. K., Agüeros, M. A., et al. 2009, *ApJS*, 182, 543, doi: [10.1088/0067-0049/182/2/543](https://doi.org/10.1088/0067-0049/182/2/543)
- Antonucci, R. 1993, *ARA&A*, 31, 473, doi: [10.1146/annurev.aa.31.090193.002353](https://doi.org/10.1146/annurev.aa.31.090193.002353)
- Argudo-Fernández, M., Verley, S., Bergond, G., et al. 2015, *A&A*, 578, A110, doi: [10.1051/0004-6361/201526016](https://doi.org/10.1051/0004-6361/201526016)
- Armitage, P. J., & Natarajan, P. 2002, *ApJL*, 567, L9, doi: [10.1086/339770](https://doi.org/10.1086/339770)
- Bahcall, J. N., Kirhakos, S., Saxe, D. H., & Schneider, D. P. 1997, *ApJ*, 479, 642, doi: [10.1086/303926](https://doi.org/10.1086/303926)
- Baldwin, J. A., Phillips, M. M., & Terlevich, R. 1981, *PASP*, 93, 5, doi: [10.1086/130766](https://doi.org/10.1086/130766)

- Barnes, J. E., & Hernquist, L. 1992, *ARA&A*, 30, 705, doi: [10.1146/annurev.aa.30.090192.003421](https://doi.org/10.1146/annurev.aa.30.090192.003421)
- Begelman, M. C., Blandford, R. D., & Rees, M. J. 1980, *Nature*, 287, 307, doi: [10.1038/287307a0](https://doi.org/10.1038/287307a0)
- Bell, E. F., Phleps, S., Somerville, R. S., et al. 2006, *ApJ*, 652, 270, doi: [10.1086/508408](https://doi.org/10.1086/508408)
- Bennert, N., Canalizo, G., Jungwiert, B., et al. 2008, *ApJ*, 677, 846, doi: [10.1086/529068](https://doi.org/10.1086/529068)
- Blecha, L., Loeb, A., & Narayan, R. 2013, *MNRAS*, 429, 2594, doi: [10.1093/mnras/sts533](https://doi.org/10.1093/mnras/sts533)
- Boroson, T. A., & Lauer, T. R. 2009, *Nature*, 458, 53, doi: [10.1038/nature07779](https://doi.org/10.1038/nature07779)
- Capelo, P. R., Dotti, M., Volonteri, M., et al. 2017, *MNRAS*, 469, 4437, doi: [10.1093/mnras/stx1067](https://doi.org/10.1093/mnras/stx1067)
- Ciotti, L., & Ostriker, J. P. 2007, *ApJ*, 665, 1038, doi: [10.1086/519833](https://doi.org/10.1086/519833)
- Ciotti, L., Ostriker, J. P., & Proga, D. 2010, *ApJ*, 717, 708, doi: [10.1088/0004-637X/717/2/708](https://doi.org/10.1088/0004-637X/717/2/708)
- Dahari, O. 1984, *AJ*, 89, 966, doi: [10.1086/113591](https://doi.org/10.1086/113591)
- . 1985, *ApJS*, 57, 643, doi: [10.1086/191021](https://doi.org/10.1086/191021)
- Darg, D. W., Kaviraj, S., Lintott, C. J., et al. 2010, *MNRAS*, 401, 1043, doi: [10.1111/j.1365-2966.2009.15686.x](https://doi.org/10.1111/j.1365-2966.2009.15686.x)
- De Rosa, A., Vignali, C., Bogdanović, T., et al. 2020, arXiv e-prints, arXiv:2001.06293. <https://arxiv.org/abs/2001.06293>
- Di Matteo, T., Springel, V., & Hernquist, L. 2005, *Nature*, 433, 604, doi: [10.1038/nature03335](https://doi.org/10.1038/nature03335)
- Doe, S., Nguyen, D., Stawarz, C., et al. 2007, *Astronomical Society of the Pacific Conference Series*, Vol. 376, *Developing Sherpa with Python*, ed. R. A. Shaw, F. Hill, & D. J. Bell, 543
- Donley, J. L., Kartaltepe, J., Kocevski, D., et al. 2018, *ApJ*, 853, 63, doi: [10.3847/1538-4357/aa9ffa](https://doi.org/10.3847/1538-4357/aa9ffa)
- Donoso, E., Yan, L., Tsai, C., et al. 2012, *ApJ*, 748, 80, doi: [10.1088/0004-637X/748/2/80](https://doi.org/10.1088/0004-637X/748/2/80)
- D’Orazio, D. J., Haiman, Z., & Schiminovich, D. 2015, *Nature*, 525, 351, doi: [10.1038/nature15262](https://doi.org/10.1038/nature15262)
- Dotti, M., Colpi, M., Haardt, F., & Mayer, L. 2007, *MNRAS*, 379, 956, doi: [10.1111/j.1365-2966.2007.12010.x](https://doi.org/10.1111/j.1365-2966.2007.12010.x)
- Dotti, M., Sesana, A., & Decarli, R. 2012, *Advances in Astronomy*, 2012, doi: [10.1155/2012/940568](https://doi.org/10.1155/2012/940568)
- Ellison, S. L., Patton, D. R., Mendel, J. T., & Scudder, J. M. 2011, *MNRAS*, 418, 2043, doi: [10.1111/j.1365-2966.2011.19624.x](https://doi.org/10.1111/j.1365-2966.2011.19624.x)
- Ellison, S. L., Patton, D. R., Simard, L., & McConnachie, A. W. 2008, *AJ*, 135, 1877, doi: [10.1088/0004-6256/135/5/1877](https://doi.org/10.1088/0004-6256/135/5/1877)
- Eracleous, M., Boroson, T. A., Halpern, J. P., & Liu, J. 2012, *ApJS*, 201, 23, doi: [10.1088/0067-0049/201/2/23](https://doi.org/10.1088/0067-0049/201/2/23)
- Faber, S. M., Tremaine, S., Ajhar, E. A., et al. 1997, *AJ*, 114, 1771, doi: [10.1086/118606](https://doi.org/10.1086/118606)
- Feigelson, E. D., & Nelson, P. I. 1985, *ApJ*, 293, 192, doi: [10.1086/163225](https://doi.org/10.1086/163225)
- Freeman, P., Doe, S., & Siemiginowska, A. 2001, in *Society of Photo-Optical Instrumentation Engineers (SPIE) Conference Series*, Vol. 4477, *Society of Photo-Optical Instrumentation Engineers (SPIE) Conference Series*, ed. J.-L. Starck & F. D. Murtagh, 76–87, doi: [10.1117/12.447161](https://doi.org/10.1117/12.447161)
- Fruscione, A., McDowell, J. C., Allen, G. E., et al. 2006, in *Society of Photo-Optical Instrumentation Engineers (SPIE) Conference Series*, Vol. 6270, *Society of Photo-Optical Instrumentation Engineers (SPIE) Conference Series*, doi: [10.1117/12.671760](https://doi.org/10.1117/12.671760)
- Gandhi, P., Horst, H., Smette, A., et al. 2009, *A&A*, 502, 457, doi: [10.1051/0004-6361/200811368](https://doi.org/10.1051/0004-6361/200811368)
- Gaskell, C. M. 1982, *ApJ*, 263, 79, doi: [10.1086/160481](https://doi.org/10.1086/160481)
- Germain, G., Milaszewski, R., McLaughlin, W., et al. 2006, *Astronomical Society of the Pacific Conference Series*, Vol. 351, *ChIPS - CIAO’s New Visualization Plotting Package*, ed. C. Gabriel, C. Arviset, D. Ponz, & S. Enrique, 57
- Graham, A. W. 2004, *ApJL*, 613, L33, doi: [10.1086/424928](https://doi.org/10.1086/424928)
- Graham, M. J., Djorgovski, S. G., Stern, D., et al. 2015a, *MNRAS*, 453, 1562, doi: [10.1093/mnras/stv1726](https://doi.org/10.1093/mnras/stv1726)
- . 2015b, *Nature*, 518, 74, doi: [10.1038/nature14143](https://doi.org/10.1038/nature14143)
- Green, P. J., Myers, A. D., Barkhouse, W. A., et al. 2010, *ApJ*, 710, 1578, doi: [10.1088/0004-637X/710/2/1578](https://doi.org/10.1088/0004-637X/710/2/1578)
- Grogin, N. A., Conselice, C. J., Chatzichristou, E., et al. 2005, *ApJL*, 627, L97, doi: [10.1086/432256](https://doi.org/10.1086/432256)

- Gross, A. C., Fu, H., Myers, A. D., Wrobel, J. M., & Djorgovski, S. G. 2019, *ApJ*, 883, 50, doi: [10.3847/1538-4357/ab3795](https://doi.org/10.3847/1538-4357/ab3795)
- Gültekin, K., Richstone, D. O., Gebhardt, K., et al. 2009, *ApJ*, 698, 198, doi: [10.1088/0004-637X/698/1/198](https://doi.org/10.1088/0004-637X/698/1/198)
- Heckman, T. M., Ptak, A., Hornschemeier, A., & Kauffmann, G. 2005, *ApJ*, 634, 161, doi: [10.1086/491665](https://doi.org/10.1086/491665)
- Hennawi, J. F., Strauss, M. A., Oguri, M., et al. 2006, *AJ*, 131, 1, doi: [10.1086/498235](https://doi.org/10.1086/498235)
- Hennawi, J. F., Myers, A. D., Shen, Y., et al. 2010, *ApJ*, 719, 1672, doi: [10.1088/0004-637X/719/2/1672](https://doi.org/10.1088/0004-637X/719/2/1672)
- Hernquist, L. 1989, *Nature*, 340, 687, doi: [10.1038/340687a0](https://doi.org/10.1038/340687a0)
- Ho, L. C. 2008, *ARA&A*, 46, 475, doi: [10.1146/annurev.astro.45.051806.110546](https://doi.org/10.1146/annurev.astro.45.051806.110546)
- Hopkins, P. F., Hernquist, L., Cox, T. J., & Kereš, D. 2008, *ApJS*, 175, 356, doi: [10.1086/524362](https://doi.org/10.1086/524362)
- Hopkins, P. F., Kocevski, D. D., & Bundy, K. 2014, *MNRAS*, 445, 823, doi: [10.1093/mnras/stu1736](https://doi.org/10.1093/mnras/stu1736)
- Hou, M., Li, Z., Peng, E. W., & Liu, C. 2017, *ApJ*, 846, 126, doi: [10.3847/1538-4357/aa8635](https://doi.org/10.3847/1538-4357/aa8635)
- Hou, M., Liu, X., Guo, H., et al. 2019, *ApJ*, 882, 41, doi: [10.3847/1538-4357/ab3225](https://doi.org/10.3847/1538-4357/ab3225)
- Hutchings, J. B., & Campbell, B. 1983, *Nature*, 303, 584, doi: [10.1038/303584a0](https://doi.org/10.1038/303584a0)
- Jin, X., Hou, M., Zhu, Z., & Li, Z. 2019, *ApJ*, 876, 53, doi: [10.3847/1538-4357/ab064f](https://doi.org/10.3847/1538-4357/ab064f)
- Kashyap, V. L., van Dyk, D. A., Connors, A., et al. 2010, *ApJ*, 719, 900, doi: [10.1088/0004-637X/719/1/900](https://doi.org/10.1088/0004-637X/719/1/900)
- Kauffmann, G., & Haehnelt, M. 2000, *MNRAS*, 311, 576, doi: [10.1046/j.1365-8711.2000.03077.x](https://doi.org/10.1046/j.1365-8711.2000.03077.x)
- Kauffmann, G., & Heckman, T. M. 2009, *MNRAS*, 397, 135, doi: [10.1111/j.1365-2966.2009.14960.x](https://doi.org/10.1111/j.1365-2966.2009.14960.x)
- Kauffmann, G., Heckman, T. M., Tremonti, C., et al. 2003, *MNRAS*, 346, 1055, doi: [10.1111/j.1365-2966.2003.07154.x](https://doi.org/10.1111/j.1365-2966.2003.07154.x)
- Keel, W. C., Kennicutt, Jr., R. C., Hummel, E., & van der Hulst, J. M. 1985, *AJ*, 90, 708, doi: [10.1086/113779](https://doi.org/10.1086/113779)
- Kennicutt, Jr., R. C., & Keel, W. C. 1984, *ApJL*, 279, L5, doi: [10.1086/184243](https://doi.org/10.1086/184243)
- Kewley, L. J., Dopita, M. A., Sutherland, R. S., Heisler, C. A., & Trevena, J. 2001, *ApJ*, 556, 121, doi: [10.1086/321545](https://doi.org/10.1086/321545)
- Khachikian, E. Y. 1987, in *IAU Symposium*, Vol. 121, *Observational Evidence of Activity in Galaxies*, ed. E. E. Khachikian, K. J. Fricke, & J. Melnick, 65–+
- Komossa, S., Burwitz, V., Hasinger, G., et al. 2003, *ApJL*, 582, L15, doi: [10.1086/346145](https://doi.org/10.1086/346145)
- Kormendy, J., Fisher, D. B., Cornell, M. E., & Bender, R. 2009, *ApJS*, 182, 216, doi: [10.1088/0067-0049/182/1/216](https://doi.org/10.1088/0067-0049/182/1/216)
- Kormendy, J., & Richstone, D. 1995, *ARA&A*, 33, 581, doi: [10.1146/annurev.aa.33.090195.003053](https://doi.org/10.1146/annurev.aa.33.090195.003053)
- Koss, M., Mushotzky, R., Treister, E., et al. 2012, *ApJL*, 746, L22, doi: [10.1088/2041-8205/746/2/L22](https://doi.org/10.1088/2041-8205/746/2/L22)
- Koss, M., Mushotzky, R., Veilleux, S., & Winter, L. 2010, *ApJL*, 716, L125, doi: [10.1088/2041-8205/716/2/L125](https://doi.org/10.1088/2041-8205/716/2/L125)
- Koss, M. J., Glidden, A., Baloković, M., et al. 2016, *ApJL*, 824, L4, doi: [10.3847/2041-8205/824/1/L4](https://doi.org/10.3847/2041-8205/824/1/L4)
- Lamastra, A., Bianchi, S., Matt, G., et al. 2009, *A&A*, 504, 73, doi: [10.1051/0004-6361/200912023](https://doi.org/10.1051/0004-6361/200912023)
- Lauer, T. R., Faber, S. M., Gebhardt, K., et al. 2005, *AJ*, 129, 2138, doi: [10.1086/429565](https://doi.org/10.1086/429565)
- Lehmer, B. D., Alexander, D. M., Bauer, F. E., et al. 2010, *ApJ*, 724, 559, doi: [10.1088/0004-637X/724/1/559](https://doi.org/10.1088/0004-637X/724/1/559)
- Li, C., Kauffmann, G., Heckman, T. M., White, S. D. M., & Jing, Y. P. 2008, *MNRAS*, 385, 1915, doi: [10.1111/j.1365-2966.2008.13023.x](https://doi.org/10.1111/j.1365-2966.2008.13023.x)
- Liu, X., Civano, F., Shen, Y., et al. 2013, *ApJ*, 762, 110, doi: [10.1088/0004-637X/762/2/110](https://doi.org/10.1088/0004-637X/762/2/110)
- Liu, X., Shen, Y., Bian, F., Loeb, A., & Tremaine, S. 2014, *ApJ*, 789, 140, doi: [10.1088/0004-637X/789/2/140](https://doi.org/10.1088/0004-637X/789/2/140)
- Liu, X., Shen, Y., & Strauss, M. A. 2011a, *ApJL*, 736, L7+, doi: [10.1088/2041-8205/736/1/L7](https://doi.org/10.1088/2041-8205/736/1/L7)
- . 2012, *ApJ*, 745, 94, doi: [10.1088/0004-637X/745/1/94](https://doi.org/10.1088/0004-637X/745/1/94)
- Liu, X., Shen, Y., Strauss, M. A., & Hao, L. 2011b, *ApJ*, 737, 101, doi: [10.1088/0004-637X/737/2/101](https://doi.org/10.1088/0004-637X/737/2/101)
- Liu, X., Hou, M., Li, Z., et al. 2019, *ApJ*, 887, 90, doi: [10.3847/1538-4357/ab54c3](https://doi.org/10.3847/1538-4357/ab54c3)
- Lutz, D., Veilleux, S., & Genzel, R. 1999, *ApJL*, 517, L13, doi: [10.1086/312014](https://doi.org/10.1086/312014)
- Mazzarella, J. M., Iwasawa, K., Vavilkin, T., et al. 2012, *AJ*, 144, 125, doi: [10.1088/0004-6256/144/5/125](https://doi.org/10.1088/0004-6256/144/5/125)

- Menci, N., Gatti, M., Fiore, F., & Lamastra, A. 2014, *A&A*, 569, A37, doi: [10.1051/0004-6361/201424217](https://doi.org/10.1051/0004-6361/201424217)
- Merritt, D. 2013, *Dynamics and Evolution of Galactic Nuclei*, Princeton Series in Astrophysics (Princeton University Press). <http://books.google.com/books?id=cOa1ku640zAC>
- Merritt, D., & Ekers, R. D. 2002, *Science*, 297, 1310, doi: [10.1126/science.1074688](https://doi.org/10.1126/science.1074688)
- Merritt, D., Milosavljević, M., Favata, M., Hughes, S. A., & Holz, D. E. 2004, *ApJL*, 607, L9, doi: [10.1086/421551](https://doi.org/10.1086/421551)
- Mihos, J. C., & Hernquist, L. 1996, *ApJ*, 464, 641, doi: [10.1086/177353](https://doi.org/10.1086/177353)
- Miller, C. J., Nichol, R. C., Gómez, P. L., Hopkins, A. M., & Bernardi, M. 2003, *ApJ*, 597, 142, doi: [10.1086/378383](https://doi.org/10.1086/378383)
- Milosavljević, M., & Merritt, D. 2001, *ApJ*, 563, 34, doi: [10.1086/323830](https://doi.org/10.1086/323830)
- Moore, B., Katz, N., Lake, G., Dressler, A., & Oemler, A. 1996, *Nature*, 379, 613, doi: [10.1038/379613a0](https://doi.org/10.1038/379613a0)
- Myers, A. D., Richards, G. T., Brunner, R. J., et al. 2008, *ApJ*, 678, 635, doi: [10.1086/533491](https://doi.org/10.1086/533491)
- Norman, C., & Scoville, N. 1988, *ApJ*, 332, 124, doi: [10.1086/166637](https://doi.org/10.1086/166637)
- Panessa, F., Bassani, L., Cappi, M., et al. 2006, *A&A*, 455, 173, doi: [10.1051/0004-6361:20064894](https://doi.org/10.1051/0004-6361:20064894)
- Park, T., Kashyap, V. L., Siemiginowska, A., et al. 2006, *ApJ*, 652, 610, doi: [10.1086/507406](https://doi.org/10.1086/507406)
- Petrosian, A. R. 1982, *Astrofizika*, 18, 548
- Pfeifle, R. W., Satyapal, S., Manzano-King, C., et al. 2019a, *ApJ*, 883, 167, doi: [10.3847/1538-4357/ab3a9b](https://doi.org/10.3847/1538-4357/ab3a9b)
- Pfeifle, R. W., Satyapal, S., Secrest, N. J., et al. 2019b, *ApJ*, 875, 117, doi: [10.3847/1538-4357/ab07bc](https://doi.org/10.3847/1538-4357/ab07bc)
- Pierce, C. M., Lotz, J. M., Laird, E. S., et al. 2007, *ApJL*, 660, L19, doi: [10.1086/517922](https://doi.org/10.1086/517922)
- Ranalli, P., Comastri, A., & Setti, G. 2003, *A&A*, 399, 39, doi: [10.1051/0004-6361:20021600](https://doi.org/10.1051/0004-6361:20021600)
- Richards, G. T., Strauss, M. A., Fan, X., et al. 2006, *AJ*, 131, 2766, doi: [10.1086/503559](https://doi.org/10.1086/503559)
- Richstone, D., Ajhar, E. A., Bender, R., et al. 1998, *Nature*, 395, A14+
- Rosas-Guevara, Y. M., Bower, R. G., McAlpine, S., Bonoli, S., & Tissera, P. B. 2019, *MNRAS*, 483, 2712, doi: [10.1093/mnras/sty3251](https://doi.org/10.1093/mnras/sty3251)
- Sanders, D. B., & Mirabel, I. F. 1996, *ARA&A*, 34, 749, doi: [10.1146/annurev.astro.34.1.749](https://doi.org/10.1146/annurev.astro.34.1.749)
- Sanders, D. B., Soifer, B. T., Elias, J. H., et al. 1988, *ApJ*, 325, 74, doi: [10.1086/165983](https://doi.org/10.1086/165983)
- Satyapal, S., Secrest, N. J., Ricci, C., et al. 2017, *ApJ*, 848, 126, doi: [10.3847/1538-4357/aa88ca](https://doi.org/10.3847/1538-4357/aa88ca)
- Schmitt, H. R. 2001, *AJ*, 122, 2243, doi: [10.1086/323547](https://doi.org/10.1086/323547)
- Serber, W., Bahcall, N., Ménard, B., & Richards, G. 2006, *ApJ*, 643, 68, doi: [10.1086/501443](https://doi.org/10.1086/501443)
- Shen, Y. 2009, *ApJ*, 704, 89, doi: [10.1088/0004-637X/704/1/89](https://doi.org/10.1088/0004-637X/704/1/89)
- Shen, Y., Liu, X., Loeb, A., & Tremaine, S. 2013, *ApJ*, 775, 49, doi: [10.1088/0004-637X/775/1/49](https://doi.org/10.1088/0004-637X/775/1/49)
- Shen, Y., & Loeb, A. 2010, *ApJ*, 725, 249, doi: [10.1088/0004-637X/725/1/249](https://doi.org/10.1088/0004-637X/725/1/249)
- Shen, Y., Hennawi, J. F., Shankar, F., et al. 2010, *ApJ*, 719, 1693, doi: [10.1088/0004-637X/719/2/1693](https://doi.org/10.1088/0004-637X/719/2/1693)
- Shlosman, I., Begelman, M. C., & Frank, J. 1990, *Nature*, 345, 679, doi: [10.1038/345679a0](https://doi.org/10.1038/345679a0)
- Silverman, J. D., Kampeczyk, P., Jahnke, K., et al. 2011, *ApJ*, 743, 2, doi: [10.1088/0004-637X/743/1/2](https://doi.org/10.1088/0004-637X/743/1/2)
- Solanes, J. M., Perea, J. D., Valentí-Rojas, G., et al. 2019, *A&A*, 624, A86, doi: [10.1051/0004-6361/201833767](https://doi.org/10.1051/0004-6361/201833767)
- Tananbaum, H., Weisskopf, M. C., Tucker, W., Wilkes, B., & Edmonds, P. 2014, *Reports on Progress in Physics*, 77, 066902, doi: [10.1088/0034-4885/77/6/066902](https://doi.org/10.1088/0034-4885/77/6/066902)
- Teng, S. H., Schawinski, K., Urry, C. M., et al. 2012, *ApJ*, 753, 165, doi: [10.1088/0004-637X/753/2/165](https://doi.org/10.1088/0004-637X/753/2/165)
- Terashima, Y., Ho, L. C., & Ptak, A. F. 2000, *ApJ*, 539, 161, doi: [10.1086/309234](https://doi.org/10.1086/309234)
- Toomre, A., & Toomre, J. 1972, *ApJ*, 178, 623, doi: [10.1086/151823](https://doi.org/10.1086/151823)
- Treister, E., Schawinski, K., Urry, C. M., & Simmons, B. D. 2012, *ApJL*, 758, L39, doi: [10.1088/2041-8205/758/2/L39](https://doi.org/10.1088/2041-8205/758/2/L39)
- Veilleux, S., & Osterbrock, D. E. 1987, *ApJS*, 63, 295, doi: [10.1086/191166](https://doi.org/10.1086/191166)
- Vignali, C., Piconcelli, E., Perna, M., et al. 2018, *MNRAS*, 477, 780, doi: [10.1093/mnras/sty682](https://doi.org/10.1093/mnras/sty682)
- Villforth, C., Hamann, F., Rosario, D. J., et al. 2014, *MNRAS*, 439, 3342, doi: [10.1093/mnras/stu173](https://doi.org/10.1093/mnras/stu173)

- Villforth, C., Hamilton, T., Pawlik, M. M., et al. 2017, MNRAS, 466, 812, doi: [10.1093/mnras/stw3037](https://doi.org/10.1093/mnras/stw3037)
- Vorontsov-Velyaminov, B. A. 1959, in Atlas and catalog of interacting galaxies (1959), 0–+
- Wada, K. 2004, *Coevolution of Black Holes and Galaxies*, Published by Cambridge University Press, 186
- Wang, L., Greene, J. E., Ju, W., et al. 2017, ApJ, 834, 129, doi: [10.3847/1538-4357/834/2/129](https://doi.org/10.3847/1538-4357/834/2/129)
- Waskett, T. J., Eales, S. A., Gear, W. K., et al. 2005, MNRAS, 363, 801, doi: [10.1111/j.1365-2966.2005.09480.x](https://doi.org/10.1111/j.1365-2966.2005.09480.x)
- Wright, E. L., Eisenhardt, P. R. M., Mainzer, A. K., et al. 2010, AJ, 140, 1868, doi: [10.1088/0004-6256/140/6/1868](https://doi.org/10.1088/0004-6256/140/6/1868)
- Yan, R., & Blanton, M. R. 2012, ApJ, 747, 61, doi: [10.1088/0004-637X/747/1/61](https://doi.org/10.1088/0004-637X/747/1/61)
- Yang, C., Ge, J., & Lu, Y. 2019a, *Science China Physics, Mechanics, and Astronomy*, 62, 129511, doi: [10.1007/s11433-019-9442-9](https://doi.org/10.1007/s11433-019-9442-9)
- Yang, C., Ge, J.-Q., & Lu, Y.-J. 2019b, *Research in Astronomy and Astrophysics*, 19, 177, doi: [10.1088/1674-4527/19/12/177](https://doi.org/10.1088/1674-4527/19/12/177)
- Yu, Q. 2002, MNRAS, 331, 935, doi: [10.1046/j.1365-8711.2002.05242.x](https://doi.org/10.1046/j.1365-8711.2002.05242.x)
- Zwicky, F. 1956, *Ergebnisse der exakten Naturwissenschaften*, 29, 344

Table 1. Information of AGN pairs with *Chandra* observation

Name (1)	R.A. (2)	Dec. (3)	z (4)	r_p (5)	$\log M_*$ (6)	$F_{[\text{O III}]}$ (7)	SFR (8)	ObsID (9)	Instr. (10)	Exp. (11)	$\log L_{X,\text{lim}}$ (12)	flag (13)
J145059.71-000215.2	222.74879	-0.03756	0.0429	2.3	11.4	103.2 ± 7.8	$0.11^{+0.45}_{-0.11}$	14008	ACIS-I	25.1	40.26	1
J145059.84-000213.2	222.74933	-0.03700	0.0430	2.3	9.7	29.1 ± 6.7	$0.02^{+0.10}_{-0.02}$	14008	ACIS-I	25.1	40.27	1
J102700.40+174901.0	156.75167	17.81694	0.0665	3.0	10.9	72.3 ± 5.9	$1.09^{+3.04}_{-0.97}$	14971	ACIS-S	49.1	40.35	0
J102700.56+174900.3	156.75233	17.81675	0.0666	3.0	...	95.1 ± 2.5	$12.86^{+29.44}_{-9.38}$	14971	ACIS-S	49.1	40.35	1
J085837.53+182221.6	134.65637	18.37267	0.0587	3.3	10.4	399.7 ± 6.3	$3.55^{+8.31}_{-2.62}$	14970	ACIS-S	19.8	40.49	1
J085837.68+182223.4	134.65700	18.37317	0.0589	3.3	11.1	1096.4 ± 11.7	$3.46^{+9.05}_{-2.88}$	14970	ACIS-S	19.8	40.49	1
J154403.45+044607.5	236.01437	4.76875	0.0420	3.4	9.8	137.4 ± 5.3	$0.37^{+1.09}_{-0.34}$	14968	ACIS-S	14.9	40.32	1
J154403.67+044610.1	236.01529	4.76947	0.0416	3.4	11.1	232.2 ± 4.6	$0.91^{+2.27}_{-0.72}$	14968	ACIS-S	14.9	40.31	1
J105842.44+314457.6	164.67683	31.74933	0.0728	4.1	10.0	225.0 ± 5.2	$1.95^{+2.73}_{-1.19}$	14966	ACIS-S	14.5	40.82	1
J105842.58+314459.8	164.67742	31.74994	0.0723	4.1	10.9	619.8 ± 8.4	$2.44^{+5.33}_{-1.75}$	14966	ACIS-S	14.5	40.81	1
J002208.69+002200.5	5.53621	0.36681	0.0710	4.2	11.0	25.9 ± 4.3	$0.02^{+0.15}_{-0.02}$	2252	ACIS-I	70.9	40.43	1
J002208.83+002202.8	5.53679	0.36744	0.0707	4.2	11.2	18.5 ± 3.2	$0.03^{+0.16}_{-0.02}$	2252	ACIS-I	70.9	40.43	1
J220634.97+000327.6	331.64571	0.05767	0.0466	4.3	...	85.3 ± 5.9	$0.68^{+1.58}_{-0.50}$	19454	ACIS-S	15.9	40.47	0
J220635.08+000323.2	331.64617	0.05644	0.0461	4.3	...	290.4 ± 6.9	$0.74^{+1.86}_{-0.59}$	19454	ACIS-S	15.9	40.46	1
J133031.75-003611.9	202.63229	-0.60331	0.0542	4.4	8.8	233.0 ± 4.3	$0.35^{+0.49}_{-0.21}$	14967	ACIS-S	14.9	40.54	0
J133032.00-003613.5	202.63333	-0.60375	0.0542	4.4	10.7	815.4 ± 9.7	$4.58^{+7.86}_{-2.98}$	14967	ACIS-S	14.9	40.54	1
J121345.95+024839.0	183.44146	2.81083	0.0730	4.8	10.4	42.6 ± 2.6	$9.29^{+19.88}_{-6.59}$	4110	ACIS-S	10.0	40.86	1
J121346.11+024841.4	183.44212	2.81150	0.0731	4.8	10.6	230.8 ± 4.1	$13.28^{+17.60}_{-7.80}$	4110	ACIS-S	10.0	40.86	1
J141447.15-000013.3	213.69646	-0.00369	0.0475	4.9	10.5	647.2 ± 7.1	$0.27^{+0.77}_{-0.24}$	17149	ACIS-I	67.0	40.03	1
J141447.48-000011.3	213.69783	-0.00314	0.0474	4.9	10.2	148.2 ± 4.3	$3.54^{+4.94}_{-2.12}$	17149	ACIS-I	67.0	40.02	1
J080523.29+281815.8	121.34704	28.30439	0.1284	5.6	11.2	2910.7 ± 18.4	$11.68^{+15.90}_{-6.95}$	14964	ACIS-S	14.0	41.35	1
J080523.40+281814.1	121.34750	28.30392	0.1286	5.6	9.8	257.3 ± 6.5	$2.24^{+3.31}_{-1.38}$	14964	ACIS-S	14.0	41.35	0
J133817.27+481632.3	204.57196	48.27564	0.0278	6.4	10.0	4901.8 ± 34.8	$5.48^{+7.89}_{-3.33}$	2044	ACIS-S	10.9	40.06	1
J133817.77+481641.1	204.57404	48.27808	0.0277	6.4	10.6	4142.2 ± 31.6	$2.84^{+3.66}_{-1.66}$	2044	ACIS-S	10.9	40.05	1
J114753.63+094552.0	176.97346	9.76444	0.0951	6.6	10.3	1368.1 ± 13.0	$8.63^{+14.39}_{-5.58}$	18198	ACIS-S	22.6	41.00	1
J114753.68+094555.6	176.97367	9.76544	0.0966	6.6	11.0	35.7 ± 5.8	$1.10^{+1.56}_{-0.63}$	18198	ACIS-S	22.6	41.01	0
J005113.94+002047.2	12.80808	0.34644	0.1124	6.9	...	55.4 ± 3.0	$3.19^{+6.38}_{-2.21}$	19453	ACIS-S	28.7	41.01	1
J005114.12+002049.2	12.80883	0.34700	0.1126	6.9	11.0	31.5 ± 1.5	$8.23^{+24.20}_{-6.63}$	19453	ACIS-S	28.7	41.01	1
J085312.36+162619.5	133.30150	16.43875	0.0637	8.0	10.5	278.0 ± 6.3	$3.57^{+4.88}_{-2.12}$	12143	ACIS-S	9.9	40.78	1
J085312.70+162615.5	133.30292	16.43764	0.0649	8.0	9.9	362.6 ± 3.9	$0.32^{+0.49}_{-0.20}$	12143	ACIS-S	9.9	40.80	1
J083847.57+040734.6	129.69821	4.12628	0.0484	8.1	9.9	27.7 ± 3.3	$0.24^{+0.58}_{-0.18}$	18159	ACIS-S	14.8	40.50	0
J083848.15+040734.1	129.70062	4.12614	0.0476	8.1	10.8	2413.7 ± 23.7	$0.66^{+1.67}_{-0.53}$	18159	ACIS-S	14.8	40.49	1
J083817.59+305453.5	129.57329	30.91486	0.0478	8.8	10.7	80.2 ± 4.5	$2.62^{+5.73}_{-1.88}$	12817	ACIS-I	4.9	40.93	1
J083817.95+305501.1	129.57479	30.91697	0.0481	8.8	11.2	20.9 ± 4.9	$0.05^{+0.28}_{-0.04}$	12817	ACIS-I	4.9	40.94	0
J090714.45+520343.4	136.81021	52.06206	0.0596	8.9	10.6	436.2 ± 6.2	$0.59^{+1.61}_{-0.52}$	14965	ACIS-S	14.5	40.64	1
J090714.61+520350.7	136.81087	52.06408	0.0602	8.9	10.3	325.1 ± 3.4	$1.28^{+2.95}_{-0.94}$	14965	ACIS-S	14.5	40.65	1
J134736.41+173404.7	206.90171	17.56797	0.0447	9.3	9.4	1681.9 ± 13.7	$0.30^{+0.41}_{-0.18}$	10561	ACIS-S	1.7	41.17	1
J134737.11+173404.1	206.90462	17.56781	0.0450	9.3	10.5	23.1 ± 2.8	$0.13^{+0.35}_{-0.11}$	10561	ACIS-S	1.7	41.17	0
J000249.07+004504.8	0.70446	0.75133	0.0868	9.5	11.2	1037.7 ± 11.6	$0.16^{+0.97}_{-0.15}$	4861	ACIS-S	5.0	41.43	1
J000249.44+004506.7	0.70600	0.75186	0.0865	9.5	10.9	17.1 ± 3.9	$0.01^{+0.09}_{-0.01}$	4861	ACIS-S	5.0	41.43	0
J135429.06+132757.3	208.62108	13.46592	0.0633	12.5	10.1	3422.6 ± 25.5	$0.04^{+0.12}_{-0.04}$	16115	ACIS-S	9.1	40.86	1
J135429.18+132807.4	208.62158	13.46872	0.0634	12.5	10.7	187.2 ± 4.1	$0.64^{+1.66}_{-0.52}$	16115	ACIS-S	9.1	40.86	0
J135225.64+142919.3	208.10683	14.48869	0.0415	14.1	10.7	45.6 ± 5.7	$0.01^{+0.07}_{-0.01}$	12822	ACIS-I	4.9	40.86	0

Table 1 continued on next page

Table 1 (continued)

Name	R.A.	Dec.	z	r_p	$\log M_*$	$F_{[\text{O III}]}$	SFR	ObsID	Instr.	Exp.	$\log L_{X,\text{lim}}$	flag
(1)	(2)	(3)	(4)	(5)	(6)	(7)	(8)	(9)	(10)	(11)	(12)	(13)
J135226.65+142927.5	208.11104	14.49097	0.0406	14.1	11.2	43.4 ± 5.4	$3.74^{+7.98}_{-2.65}$	12822	ACIS-I	4.9	40.84	0
J124610.11+304354.9	191.54212	30.73192	0.0219	16.4	10.9	82.2 ± 3.4	$10.61^{+19.49}_{-7.13}$	2043	ACIS-S	27.9	39.38	1
J124611.24+304321.9	191.54683	30.72275	0.0218	16.4	9.9	206.3 ± 6.9	$0.01^{+0.05}_{-0.01}$	2043	ACIS-S	27.9	39.38	1
J111519.23+542310.9	168.83012	54.38636	0.0713	17.1	10.5	345.5 ± 4.4	$0.01^{+0.04}_{-0.01}$	13902	ACIS-S	19.1	40.73	0
J111519.98+542316.7	168.83325	54.38797	0.0704	17.1	11.1	1054.1 ± 10.7	$1.72^{+5.20}_{-1.60}$	13902	ACIS-S	19.1	40.72	1
J143454.22+334934.5	218.72592	33.82625	0.0578	18.0	10.8	127.9 ± 4.5	$0.01^{+0.07}_{-0.01}$	19648	ACIS-I	24.7	40.92	0
J143454.68+334920.0	218.72783	33.82222	0.0587	18.0	10.7	16.9 ± 3.7	$0.64^{+1.82}_{-0.58}$	19648	ACIS-I	24.7	40.93	0
J111830.28+402554.0	169.62617	40.43167	0.1545	18.1	868	ACIS-I	16.5	41.47	1
J111830.68+402557.0	169.62783	40.43250	0.1559	18.1	11.0	79.5 ± 3.5	$8.53^{+22.78}_{-6.52}$	868	ACIS-I	16.5	41.48	0
J214622.41+000452.1	326.59337	0.08114	0.0754	18.7	10.4	16.8 ± 2.4	$4.72^{+10.33}_{-3.39}$	20466	ACIS-S	11.9	41.20	0
J214623.23+000456.7	326.59679	0.08242	0.0750	18.7	10.9	109.6 ± 3.6	$2.72^{+6.49}_{-2.04}$	20466	ACIS-S	11.9	41.19	1
J085441.74+305754.7	133.67392	30.96519	0.1970	20.0	11662	ACIS-S	10.4	42.05	1
J085442.11+305757.4	133.67546	30.96594	0.1956	20.0	10.9	50.2 ± 2.9	$1.89^{+4.50}_{-1.40}$	11662	ACIS-S	10.4	42.04	0
J142947.66+353427.5	217.44858	35.57431	0.0283	25.0	11.0	246.9 ± 11.8	$0.01^{+0.07}_{-0.01}$	7776	ACIS-S	13.9	40.15	1
J142950.32+353412.2	217.45967	35.57006	0.0292	25.0	10.5	26.2 ± 4.3	$0.12^{+0.50}_{-0.12}$	7776	ACIS-S	13.9	40.18	0
J155548.02+242911.9	238.95008	24.48664	0.0705	28.8	10.5	13.5 ± 2.9	$0.28^{+0.35}_{-0.14}$	3984	ACIS-S	20.0	40.72	0
J155549.45+242911.5	238.95604	24.48653	0.0705	28.8	10.5	253.8 ± 6.3	$0.39^{+1.08}_{-0.35}$	3984	ACIS-S	20.0	40.72	1
J001842.19-101613.9	4.67579	-10.27053	0.1215	32.0	10.9	17.9 ± 2.6	$1.04^{+2.84}_{-0.91}$	13823	ACIS-S	29.6	41.27	0
J001842.81-101625.1	4.67837	-10.27364	0.1220	32.0	10.9	15.9 ± 3.7	$0.50^{+1.39}_{-0.44}$	13823	ACIS-S	29.6	41.27	0
J160527.62+174858.4	241.36508	17.81622	0.0335	32.4	9.7	18.4 ± 2.2	$0.01^{+0.01}_{-0.00}$	17038	ACIS-S	7.7	40.38	0
J160527.91+174946.7	241.36629	17.82964	0.0337	32.4	10.1	37.1 ± 2.9	$0.11^{+0.31}_{-0.10}$	17038	ACIS-S	7.7	40.39	0
J125929.96+275723.2	194.87483	27.95644	0.0227	34.4	10.6	33.3 ± 8.6	$0.01^{+0.03}_{-0.00}$	13996	ACIS-I	123.1	39.77	0
J125934.12+275648.6	194.89217	27.94683	0.0240	34.4	10.6	43.8 ± 10.6	$0.08^{+0.10}_{-0.04}$	13996	ACIS-I	123.1	39.82	1
J131513.87+442426.5	198.80779	44.40736	0.0354	35.9	10.5	414.5 ± 8.3	$0.45^{+1.10}_{-0.35}$	12242	ACIS-S	29.6	39.89	1
J131517.27+442425.6	198.82196	44.40711	0.0355	35.9	10.9	2250.4 ± 21.5	$0.34^{+1.27}_{-0.33}$	12242	ACIS-S	29.6	39.89	1
J142626.63+330439.5	216.61096	33.07764	0.0636	37.1	10.4	13.6 ± 2.8	$17.39^{+44.72}_{-15.12}$	19663	ACIS-I	24.0	40.67	0
J142627.54+330412.8	216.61475	33.07022	0.0645	37.1	10.4	60.9 ± 3.0	$0.03^{+0.12}_{-0.03}$	19663	ACIS-I	24.0	40.68	1
J011544.85+001400.0	18.93687	0.23333	0.0445	39.4	10.6	252.0 ± 5.6	$0.33^{+0.91}_{-0.29}$	3204	ACIS-I	37.6	40.38	1
J011545.23+001444.6	18.93846	0.24572	0.0431	39.4	...	7.6 ± 2.2	$0.01^{+0.06}_{-0.01}$	3204	ACIS-I	37.6	40.35	0
J112545.05+144035.7	171.43771	14.67658	0.0340	49.7	11.0	108.1 ± 4.7	$17.15^{+27.03}_{-10.85}$	15053	ACIS-S	14.5	40.10	1
J112549.55+144006.6	171.45646	14.66850	0.0339	49.7	10.9	60.4 ± 3.0	$12.46^{+23.30}_{-8.40}$	15053	ACIS-S	14.5	40.09	1
J122726.27+081123.8	186.85946	8.18994	0.1185	50.0	...	10.0 ± 2.4	$2.39^{+3.12}_{-1.30}$	8060	ACIS-S	5.1	41.64	0
J122727.54+081137.0	186.86475	8.19361	0.1194	50.0	...	10.9 ± 2.4	$0.90^{+1.19}_{-0.49}$	8060	ACIS-S	5.1	41.65	0
J145806.24+013020.5	224.52600	1.50569	0.0429	51.3	11.1	92.9 ± 8.2	$0.01^{+0.09}_{-0.01}$	11325	ACIS-S	8.3	40.68	0
J145808.49+013110.9	224.53537	1.51969	0.0444	51.3	10.8	27.0 ± 3.5	$0.01^{+0.09}_{-0.01}$	11325	ACIS-S	8.3	40.71	0
J143310.55+525830.5	218.29396	52.97514	0.0476	52.3	11473	ACIS-S	1.8	41.18	1
J143312.96+525747.3	218.30400	52.96314	0.0473	52.3	10.9	93.3 ± 6.9	$0.31^{+0.90}_{-0.28}$	11473	ACIS-S	1.8	41.17	1
J032015.52+412355.1	50.06467	41.39864	0.0224	58.0	11.0	82.6 ± 10.2	$0.01^{+0.05}_{-0.01}$	12037	ACIS-I	84.6	40.04	1
J032020.97+412225.5	50.08737	41.37375	0.0237	58.0	9.8	51.2 ± 8.2	$0.00^{+0.03}_{-0.00}$	12037	ACIS-I	84.6	40.09	0
J032512.84+003711.6	51.30350	0.61989	0.1502	59.7	11.1	16.8 ± 3.7	$0.03^{+0.21}_{-0.03}$	7733	ACIS-S	4.5	41.91	1
J032513.30+003733.3	51.30542	0.62592	0.1483	59.7	10.8	55.5 ± 3.7	$0.11^{+0.46}_{-0.10}$	7733	ACIS-S	4.5	41.90	0
J135740.18+223137.7	209.41742	22.52714	0.0622	60.8	10.8	36.2 ± 3.5	$0.03^{+0.22}_{-0.03}$	20115	ACIS-S	10.0	40.88	1
J135742.12+223056.1	209.42550	22.51558	0.0621	60.8	10.8	188.3 ± 4.3	$0.53^{+1.60}_{-0.50}$	20115	ACIS-S	10.0	40.88	0
J152131.56+074425.8	230.38150	7.74050	0.0425	63.0	10.9	19.1 ± 5.1	$0.02^{+0.10}_{-0.02}$	900	ACIS-I	57.3	40.38	1
J152136.39+074420.7	230.40162	7.73908	0.0441	63.0	10.6	13.4 ± 4.2	$0.01^{+0.08}_{-0.01}$	900	ACIS-I	57.3	40.41	0

Table 1 continued on next page

Table 1 (continued)

Name	R.A.	Dec.	z	r_p	$\log M_*$	$F_{[\text{O III}]}$	SFR	ObsID	Instr.	Exp.	$\log L_{X,\text{lim}}$	flag
(1)	(2)	(3)	(4)	(5)	(6)	(7)	(8)	(9)	(10)	(11)	(12)	(13)
J155957.11+412840.0	239.98796	41.47778	0.0333	64.1	10.8	32.3 ± 4.7	$0.01^{+0.05}_{-0.01}$	9206	ACIS-S	10.0	40.24	0
J160003.55+412845.4	240.01479	41.47928	0.0335	64.1	10.9	114.4 ± 9.7	$0.03^{+0.20}_{-0.03}$	9206	ACIS-S	10.0	40.25	1
J092458.83+022519.7	141.24512	2.42214	0.0716	64.3	10.8	45.6 ± 3.3	$1.13^{+2.12}_{-0.77}$	11564	ACIS-S	21.0	40.88	1
J092501.12+022447.5	141.25467	2.41319	0.0716	64.3	10.4	7.7 ± 1.9	$0.25^{+0.31}_{-0.13}$	11564	ACIS-S	21.0	40.88	0
J160526.61+175435.6	241.36087	17.90989	0.0410	64.5	10.9	41.9 ± 4.6	$0.01^{+0.05}_{-0.01}$	17038	ACIS-S	7.7	40.56	0
J160529.43+175543.0	241.37262	17.92861	0.0400	64.5	10.9	42.7 ± 4.8	$0.16^{+0.65}_{-0.15}$	17038	ACIS-S	7.7	40.54	0
J150457.12+260058.5	226.23800	26.01625	0.0540	65.2	11.3	119.4 ± 5.4	$0.01^{+0.07}_{-0.01}$	11845	ACIS-S	56.9	40.17	1
J150501.22+260101.5	226.25508	26.01708	0.0545	65.2	10.9	10.8 ± 3.3	$0.17^{+0.23}_{-0.10}$	11845	ACIS-S	56.9	40.18	1
J123405.05+062933.2	188.52104	6.49256	0.0809	65.9	...	22.3 ± 4.4	$0.05^{+0.24}_{-0.05}$	19407	ACIS-S	8.0	41.31	0
J123407.84+062922.5	188.53267	6.48958	0.0808	65.9	...	24.6 ± 3.5	$0.03^{+0.16}_{-0.02}$	19407	ACIS-S	8.0	41.31	1
J151018.41+074219.6	227.57671	7.70544	0.0424	67.3	11.3	104.0 ± 7.1	$0.09^{+0.52}_{-0.08}$	939	ACIS-I	4.9	40.79	0
J151022.87+074304.2	227.59529	7.71783	0.0442	67.3	11.0	85.2 ± 9.6	$0.02^{+0.12}_{-0.02}$	939	ACIS-I	4.9	40.82	1
J211702.44-064507.3	319.26017	-6.75203	0.0298	71.9	10.7	24.1 ± 5.7	$0.15^{+0.39}_{-0.13}$	20435	ACIS-S	12.9	40.13	0
J211706.99-064327.9	319.27912	-6.72442	0.0292	71.9	11.1	274.2 ± 15.8	$0.98^{+2.71}_{-0.87}$	20435	ACIS-S	12.9	40.11	1
J140343.63+292045.3	210.93179	29.34592	0.0633	76.3	11.2	54.5 ± 3.9	$0.40^{+2.19}_{-0.38}$	4782	ACIS-S	2.6	41.26	1
J140345.02+292144.0	210.93758	29.36222	0.0637	76.3	11.1	618.3 ± 9.0	$3.01^{+7.72}_{-2.45}$	4782	ACIS-S	2.6	41.26	1
J121351.33+024805.8	183.46387	2.80161	0.0747	76.9	10.8	15.8 ± 2.9	$0.11^{+0.40}_{-0.11}$	4110	ACIS-S	10.0	40.88	0
J121354.87+024753.0	183.47862	2.79806	0.0743	76.9	10.7	711.8 ± 9.0	$7.65^{+10.99}_{-4.63}$	4110	ACIS-S	10.0	40.87	1
J032224.28+421721.7	50.60117	42.28936	0.0510	77.0	10.9	38.8 ± 3.0	$0.90^{+2.29}_{-0.73}$	17273	ACIS-I	5.0	41.08	0
J032227.88+421626.4	50.61617	42.27400	0.0516	77.0	9.9	928.1 ± 7.0	$2.16^{+4.12}_{-1.47}$	17273	ACIS-I	5.0	41.09	1
J160501.37+174632.5	241.25571	17.77569	0.0330	78.1	10.9	54.8 ± 8.0	$0.01^{+0.06}_{-0.01}$	20087	ACIS-I	35.1	40.40	1
J160507.89+174527.6	241.28287	17.75767	0.0334	78.1	11.3	52.8 ± 5.0	$0.05^{+0.31}_{-0.05}$	20087	ACIS-I	35.1	40.41	0
J093325.71+340253.1	143.35712	34.04808	0.0272	78.6	11.0	51.0 ± 6.6	$0.01^{+0.04}_{-0.01}$	3227	ACIS-I	34.3	39.70	1
J093334.42+340153.4	143.39342	34.03150	0.0287	78.6	9.9	5.4 ± 1.8	$0.01^{+0.01}_{-0.01}$	3227	ACIS-I	34.3	39.75	0
J104229.80+050500.2	160.62417	5.08339	0.0281	80.3	9.6	7.9 ± 1.9	$0.01^{+0.00}_{-0.00}$	13871	ACIS-S	49.0	39.58	0
J104232.05+050241.9	160.63354	5.04497	0.0272	80.3	9.2	459.3 ± 5.9	$0.06^{+0.15}_{-0.05}$	13871	ACIS-S	49.0	39.55	1
J091334.02+300223.4	138.39175	30.03983	0.0214	81.2	9.9	10.0 ± 2.5	$0.01^{+0.01}_{-0.01}$	5789	ACIS-S	17.9	39.52	0
J091339.47+295934.7	138.41446	29.99297	0.0225	81.2	11.2	300.6 ± 19.3	$0.01^{+0.04}_{-0.01}$	5789	ACIS-S	17.9	39.57	1
J004239.54-093053.8	10.66475	-9.51494	0.0574	85.7	10.8	18.8 ± 4.3	$0.19^{+0.25}_{-0.10}$	4881	ACIS-I	9.8	41.01	0
J004244.64-093102.8	10.68600	-9.51744	0.0568	85.7	10.7	15.7 ± 4.4	$0.02^{+0.10}_{-0.02}$	4881	ACIS-I	9.8	41.00	0
J215945.57-002712.0	329.93987	-0.45333	0.1273	86.6	10.9	19.9 ± 2.8	$0.11^{+0.42}_{-0.11}$	11509	ACIS-S	7.8	41.73	1
J215947.31-002644.3	329.94712	-0.44564	0.1281	86.6	...	1072.6 ± 9.5	$1.35^{+4.34}_{-1.27}$	11509	ACIS-S	7.8	41.74	1
J015303.50+010123.0	28.26458	1.02306	0.0595	88.5	10.6	15.9 ± 2.6	$0.04^{+0.17}_{-0.04}$	1448	ACIS-I	6.9	40.96	0
J015308.29+010150.7	28.28454	1.03075	0.0602	88.5	10.9	109.5 ± 4.2	$0.02^{+0.10}_{-0.01}$	1448	ACIS-I	6.9	40.97	0
J082321.67+042220.9	125.84029	4.37247	0.0311	88.7	11.4	38.3 ± 8.4	$0.01^{+0.04}_{-0.01}$	15161	ACIS-I	9.9	40.54	1
J082329.88+042333.0	125.87450	4.39250	0.0308	88.7	10.3	157.0 ± 5.8	$0.04^{+0.20}_{-0.04}$	15161	ACIS-I	9.9	40.53	0
J080529.88+241004.4	121.37450	24.16789	0.0595	89.8	11.0	46.8 ± 5.5	$0.01^{+0.09}_{-0.01}$	19496	ACIS-S	69.2	40.20	0
J080535.00+240950.3	121.39583	24.16397	0.0597	89.8	11.0	2791.1 ± 23.2	$0.02^{+0.10}_{-0.01}$	19496	ACIS-S	69.2	40.20	1
J135408.85+325434.6	208.53687	32.90961	0.0256	95.4	9.1	15.3 ± 1.2	$0.01^{+0.00}_{-0.00}$	3004	ACIS-S	7.0	40.09	0
J135419.95+325547.8	208.58312	32.92994	0.0261	95.4	10.9	1139.1 ± 17.2	$0.50^{+1.38}_{-0.45}$	3004	ACIS-S	7.0	40.10	1
J102141.89+130550.4	155.42454	13.09733	0.0765	97.2	10.7	148.8 ± 3.3	$6.29^{+15.73}_{-4.83}$	4107	ACIS-S	5.4	41.10	0
J102142.79+130656.1	155.42829	13.11558	0.0763	97.2	11.1	25.4 ± 3.1	$14.83^{+35.11}_{-11.04}$	4107	ACIS-S	5.4	41.09	0
J125939.94+312707.4	194.91642	31.45206	0.0514	97.3	10.7	34.3 ± 4.0	$0.08^{+0.35}_{-0.07}$	9395	ACIS-I	17.6	40.70	1
J125946.28+312726.5	194.94283	31.45736	0.0508	97.3	10.5	15.6 ± 3.5	$0.01^{+0.05}_{-0.01}$	9395	ACIS-I	17.6	40.69	0
J141503.63+520434.3	213.76512	52.07619	0.0732	98.8	10.8	17.4 ± 3.1	$0.54^{+0.71}_{-0.29}$	5854	ACIS-I	49.7	40.59	0

Table 1 continued on next page

Table 1 (continued)

Name	R.A.	Dec.	z	r_p	$\log M_*$	$F_{[\text{O III}]}$	SFR	ObsID	Instr.	Exp.	$\log L_{X,\text{lim}}$	flag
(1)	(2)	(3)	(4)	(5)	(6)	(7)	(8)	(9)	(10)	(11)	(12)	(13)
J141503.92+520323.5	213.76633	52.05653	0.0730	98.8	10.7	12.6 ± 2.3	$1.57^{+3.97}_{-1.24}$	5854	ACIS-I	49.7	40.59	1

NOTE—(1) SDSS names with J2000 coordinates given in the form of "hhmmss.ss+ddmmss.s"; (2)-(3) Centroid position of the AGNs; (4) Redshift; (5) Projected physical separation of AGN in each pair, in units of kpc; (6) Stellar mass, in units of M_\odot ; (7) [O III] emission line fluxes and 1- σ uncertainties, in units of 10^{-17} erg s $^{-1}$ cm $^{-2}$; (8) Star formation rate, in units of M_\odot yr $^{-1}$, given by the MPA-JHU DR7 catalog inferred from $D_n(4000)$; (9) *Chandra* observation ID; (10) *Chandra* observation instrument; (11) *Chandra* effective exposure time, in units of ks; (12) 0.5-8 keV limiting luminosity for source detection, in units of erg s $^{-1}$; (13) Flag for X-ray detection, 1 and 0 represent detection and non-detection in X-ray, respectively.

Table 2. X-ray properties of AGN pairs

Name	XR.A.	XDec.	Counts	$F_{0.5-2}$	F_{2-8}	$\log L_{0.5-2}$	$\log L_{2-10}$	HR
(1)	(2)	(3)	(4)	(5)	(6)	(7)	(8)	(9)
J145059.71-000215.2	222.74890	-0.03757	$57.6^{+8.1}_{-8.0}$	$7.62^{+1.23}_{-1.12}$	$1.31^{+0.50}_{-0.41}$	$40.86^{+0.07}_{-0.07}$	$40.63^{+0.14}_{-0.16}$	$-0.65^{+0.09}_{-0.12}$
J145059.84-000213.2	222.74933	-0.03700	$5.5^{+3.1}_{-2.5}$	< 2.20	< 1.45	< 40.32	< 40.67	$-0.19^{+0.34}_{-0.57}$
J102700.56+174900.3	156.75225	17.81680	$46.9^{+8.1}_{-7.4}$	$2.18^{+0.40}_{-0.37}$	$0.70^{+0.24}_{-0.21}$	$40.71^{+0.07}_{-0.08}$	$40.75^{+0.13}_{-0.15}$	$-0.55^{+0.11}_{-0.14}$
J085837.53+182221.6	134.65693	18.37263	$15.7^{+4.7}_{-4.0}$	$2.12^{+0.62}_{-0.53}$	< 0.97	$40.58^{+0.11}_{-0.13}$	< 40.78	$-0.96^{+0.00}_{-0.04}$
J085837.68+182223.4	134.65700	18.37317	$13.6^{+4.4}_{-3.7}$	$1.69^{+0.56}_{-0.47}$	< 1.31	$40.49^{+0.12}_{-0.14}$	< 40.91	$-0.84^{+0.04}_{-0.16}$
J154403.45+044607.5	236.01437	4.76875	$5.0^{+2.9}_{-2.2}$	$1.17^{+0.55}_{-0.43}$	< 1.72	$40.02^{+0.17}_{-0.20}$	< 40.73	$-0.74^{+0.07}_{-0.26}$
J154403.67+044610.1	236.01530	4.76934	$59.3^{+8.2}_{-8.1}$	$1.33^{+0.59}_{-0.47}$	$10.19^{+1.51}_{-1.49}$	$40.07^{+0.16}_{-0.19}$	$41.49^{+0.06}_{-0.07}$	$0.73^{+0.11}_{-0.07}$
J105842.44+314457.6	164.67689	31.74925	$2.6^{+2.3}_{-1.7}$	$0.36^{+0.36}_{-0.24}$	< 1.74	$40.01^{+0.30}_{-0.46}$	< 41.22	$-0.42^{+0.19}_{-0.58}$
J105842.58+314459.8	164.67743	31.74989	$94.0^{+10.3}_{-10.2}$	$1.18^{+0.56}_{-0.44}$	$18.20^{+2.04}_{-2.02}$	$40.52^{+0.17}_{-0.20}$	$42.24^{+0.05}_{-0.05}$	$0.85^{+0.07}_{-0.04}$
J002208.69+002200.5	5.53621	0.36681	$16.7^{+5.1}_{-4.4}$	$0.75^{+0.23}_{-0.20}$	< 0.68	$40.30^{+0.12}_{-0.13}$	< 40.79	$-0.77^{+0.08}_{-0.23}$
J002208.83+002202.8	5.53679	0.36744	$15.5^{+4.9}_{-4.3}$	$0.65^{+0.22}_{-0.19}$	< 0.78	$40.24^{+0.13}_{-0.15}$	< 40.85	$-0.65^{+0.12}_{-0.26}$
J220635.08+000323.2	331.64613	0.05650	$76.9^{+9.3}_{-9.2}$	$1.57^{+0.73}_{-0.59}$	$13.25^{+1.68}_{-1.66}$	$40.24^{+0.17}_{-0.21}$	$41.70^{+0.05}_{-0.06}$	$0.81^{+0.09}_{-0.05}$
J133032.00-003613.5	202.63348	-0.60376	$16.2^{+4.7}_{-4.0}$	$2.09^{+0.71}_{-0.59}$	$1.55^{+0.64}_{-0.54}$	$40.50^{+0.13}_{-0.15}$	$40.91^{+0.15}_{-0.19}$	$-0.20^{+0.21}_{-0.24}$
J121345.95+024839.0	183.44148	2.81086	$11.3^{+4.0}_{-3.4}$	< 3.19	$1.91^{+0.88}_{-0.71}$	< 40.96	$41.27^{+0.16}_{-0.20}$	$0.19^{+0.32}_{-0.32}$
J121346.11+024841.4	183.44183	2.81139	$14.9^{+4.5}_{-3.9}$	$1.90^{+0.76}_{-0.62}$	$1.59^{+0.81}_{-0.64}$	$40.73^{+0.15}_{-0.17}$	$41.19^{+0.18}_{-0.22}$	$-0.23^{+0.23}_{-0.29}$
J141447.15-000013.3	213.69647	-0.00376	$1198.5^{+36.6}_{-36.2}$	$27.32^{+1.44}_{-1.43}$	$40.60^{+1.52}_{-1.50}$	$41.50^{+0.02}_{-0.02}$	$42.21^{+0.02}_{-0.02}$	$0.33^{+0.03}_{-0.03}$
J141447.48-000011.3	213.69784	-0.00320	$562.2^{+25.1}_{-24.9}$	$22.69^{+1.32}_{-1.31}$	$11.83^{+0.82}_{-0.82}$	$41.42^{+0.02}_{-0.03}$	$41.67^{+0.03}_{-0.03}$	$-0.18^{+0.04}_{-0.04}$
J080523.29+281815.8	121.34708	28.30438	$30.8^{+6.2}_{-5.6}$	$3.68^{+0.95}_{-0.82}$	$2.60^{+0.85}_{-0.73}$	$41.54^{+0.10}_{-0.11}$	$41.92^{+0.12}_{-0.14}$	$-0.23^{+0.17}_{-0.19}$
J133817.27+481632.3	204.57208	48.27566	$95.2^{+10.8}_{-10.6}$	$16.18^{+2.08}_{-2.06}$	$4.99^{+1.47}_{-1.26}$	$40.80^{+0.05}_{-0.06}$	$40.82^{+0.11}_{-0.13}$	$-0.65^{+0.07}_{-0.09}$
J133817.77+481641.1	204.57415	48.27808	$205.0^{+15.3}_{-15.2}$	$25.62^{+2.53}_{-2.51}$	$27.09^{+3.11}_{-3.08}$	$41.00^{+0.04}_{-0.04}$	$41.55^{+0.05}_{-0.05}$	$-0.17^{+0.06}_{-0.08}$
J114753.63+094552.0	176.97338	9.76443	$3343.2^{+61.0}_{-60.4}$	$102.63^{+4.11}_{-4.07}$	$353.07^{+7.24}_{-7.17}$	$42.70^{+0.02}_{-0.02}$	$43.77^{+0.01}_{-0.01}$	$0.58^{+0.01}_{-0.01}$
J005113.94+002047.2	12.80803	0.34644	$33.2^{+6.4}_{-5.8}$	$2.57^{+0.59}_{-0.58}$	$1.25^{+0.42}_{-0.36}$	$41.26^{+0.09}_{-0.11}$	$41.48^{+0.13}_{-0.15}$	$-0.27^{+0.16}_{-0.19}$
J005114.12+002049.2	12.80872	0.34709	$6.4^{+3.1}_{-2.4}$	$0.39^{+0.28}_{-0.20}$	$0.34^{+0.24}_{-0.17}$	$40.43^{+0.24}_{-0.32}$	$40.92^{+0.23}_{-0.31}$	$0.02^{+0.39}_{-0.40}$
J085312.36+162619.5	133.30145	16.43874	$16.5^{+4.6}_{-4.0}$	$3.72^{+1.08}_{-0.94}$	< 2.55	$40.90^{+0.11}_{-0.13}$	< 41.27	$-0.82^{+0.04}_{-0.17}$
J085312.70+162615.5	133.30362	16.43762	$92.8^{+10.2}_{-10.1}$	$2.84^{+0.97}_{-0.82}$	$24.14^{+2.83}_{-2.80}$	$40.80^{+0.13}_{-0.15}$	$42.26^{+0.05}_{-0.05}$	$0.74^{+0.08}_{-0.06}$
J083848.15+040734.1	129.70055	4.12617	$717.9^{+28.3}_{-28.0}$	$10.48^{+1.66}_{-1.52}$	$136.41^{+5.57}_{-5.51}$	$41.09^{+0.06}_{-0.07}$	$42.74^{+0.02}_{-0.02}$	$0.86^{+0.02}_{-0.02}$
J083817.59+305453.5	129.57327	30.91486	$7.8^{+2.9}_{-2.8}$	$5.23^{+2.16}_{-2.03}$	< 5.88	$40.79^{+0.15}_{-0.21}$	< 41.38	$-0.64^{+0.09}_{-0.35}$
J090714.45+520343.4	136.81035	52.06204	$41.9^{+7.2}_{-6.5}$	$0.99^{+0.52}_{-0.40}$	$7.51^{+1.30}_{-1.29}$	$40.27^{+0.18}_{-0.22}$	$41.68^{+0.07}_{-0.08}$	$0.72^{+0.13}_{-0.08}$
J090714.61+520350.7	136.81095	52.06411	$120.9^{+11.6}_{-11.5}$	$4.82^{+1.02}_{-0.95}$	$19.25^{+2.09}_{-2.07}$	$40.96^{+0.08}_{-0.10}$	$42.10^{+0.04}_{-0.05}$	$0.55^{+0.09}_{-0.07}$
J134736.41+173404.7	206.90177	17.56804	$67.8^{+8.7}_{-8.6}$	$84.17^{+11.27}_{-11.15}$	$9.67^{+4.47}_{-4.05}$	$41.94^{+0.05}_{-0.06}$	$41.53^{+0.17}_{-0.24}$	$-0.82^{+0.05}_{-0.08}$
J000249.07+004504.8	0.70424	0.75133	$13.0^{+4.2}_{-3.6}$	$2.86^{+1.77}_{-1.33}$	$6.22^{+2.49}_{-2.04}$	$41.07^{+0.21}_{-0.27}$	$41.94^{+0.15}_{-0.17}$	$0.33^{+0.31}_{-0.23}$
J135429.06+132757.3	208.62109	13.46601	$233.1^{+16.1}_{-16.0}$	$2.74^{+1.10}_{-0.90}$	$73.81^{+5.20}_{-5.15}$	$40.76^{+0.15}_{-0.17}$	$42.73^{+0.03}_{-0.03}$	$0.92^{+0.03}_{-0.02}$
J124610.11+304354.9	191.54192	30.73191	$18.3^{+5.4}_{-4.7}$	$1.56^{+0.44}_{-0.39}$	$0.66^{+0.38}_{-0.29}$	$39.57^{+0.11}_{-0.12}$	$39.73^{+0.20}_{-0.25}$	$-0.55^{+0.15}_{-0.23}$

Table 2 continued on next page

Table 2 (continued)

Name	XR.A.	XDec.	Counts	F _{0.5-2}	F ₂₋₈	log L _{0.5-2}	log L ₂₋₁₀	HR
(1)	(2)	(3)	(4)	(5)	(6)	(7)	(8)	(9)
J124611.24+304321.9	191.54684	30.72281	70.6 ^{+9.0} _{-9.0}	3.27 ^{+0.54} _{-0.49}	2.45 ^{+0.56} _{-0.51}	39.89 ^{+0.07} _{-0.07}	40.30 ^{+0.09} _{-0.10}	-0.34 ^{+0.10} _{-0.13}
J111519.98+542316.7	168.83312	54.38791	1496.8 ^{+40.9} _{-40.4}	17.10 ^{+1.61} _{-1.60}	214.35 ^{+6.11} _{-6.05}	41.65 ^{+0.04} _{-0.04}	43.28 ^{+0.01} _{-0.01}	0.83 ^{+0.01} _{-0.02}
J111830.28+402554.0	169.62611	40.43169	1859.6 ^{+45.5} _{-45.1}	288.97 ^{+8.03} _{-7.95}	88.81 ^{+4.58} _{-4.54}	43.60 ^{+0.01} _{-0.01}	43.62 ^{+0.02} _{-0.02}	-0.55 ^{+0.02} _{-0.02}
J214623.23+000456.7	326.59679	0.08242	8.3 ^{+3.7} _{-3.0}	< 2.74	2.13 ^{+0.97} _{-0.79}	< 40.92	41.34 ^{+0.16} _{-0.20}	0.80 ^{+0.20} _{-0.04}
J085441.74+305754.7	133.67393	30.96521	556.5 ^{+24.9} _{-24.7}	155.97 ^{+8.10} _{-8.02}	52.30 ^{+4.63} _{-4.58}	43.56 ^{+0.02} _{-0.02}	43.62 ^{+0.04} _{-0.04}	-0.49 ^{+0.04} _{-0.04}
J142947.66+353427.5	217.44857	35.57429	251.6 ^{+16.8} _{-16.6}	18.99 ^{+2.39} _{-2.36}	48.03 ^{+3.79} _{-3.75}	40.89 ^{+0.05} _{-0.06}	41.82 ^{+0.03} _{-0.04}	0.43 ^{+0.06} _{-0.06}
J155549.45+242911.5	238.95602	24.48637	35.5 ^{+6.5} _{-6.1}	1.57 ^{+0.58} _{-0.48}	4.44 ^{+0.94} _{-0.87}	40.62 ^{+0.14} _{-0.16}	41.60 ^{+0.08} _{-0.10}	0.44 ^{+0.17} _{-0.13}
J125934.12+275648.6	194.89207	27.94666	59.0 ^{+12.2} _{-12.1}	2.49 ^{+0.43} _{-0.42}	< 0.61	39.86 ^{+0.07} _{-0.08}	< 39.78	-0.95 ^{+0.00} _{-0.05}
J131513.87+442426.5	198.80783	44.40742	14.5 ^{+4.5} _{-3.9}	1.03 ^{+0.34} _{-0.28}	< 1.05	39.82 ^{+0.12} _{-0.14}	< 40.36	-0.73 ^{+0.07} _{-0.24}
J131517.27+442425.6	198.82213	44.40720	3835.5 ^{+65.4} _{-64.8}	17.35 ^{+1.26} _{-1.24}	363.46 ^{+6.37} _{-6.31}	41.05 ^{+0.03} _{-0.03}	42.90 ^{+0.01} _{-0.01}	0.89 ^{+0.01} _{-0.01}
J142627.54+330412.8	216.61463	33.07008	2.1 ^{+2.0} _{-1.3}	< 2.28	< 1.53	< 40.70	< 41.06	-0.04 ^{+0.56} _{-0.61}
J011544.85+001400.0	18.93686	0.23343	367.9 ^{+20.4} _{-20.2}	29.79 ^{+2.05} _{-2.03}	16.68 ^{+1.55} _{-1.54}	41.48 ^{+0.03} _{-0.03}	41.76 ^{+0.04} _{-0.04}	-0.28 ^{+0.05} _{-0.05}
J112545.05+144035.7	171.43785	14.67653	25.2 ^{+5.7} _{-5.0}	4.16 ^{+1.01} _{-0.89}	0.68 ^{+0.47} _{-0.34}	40.39 ^{+0.09} _{-0.10}	40.13 ^{+0.23} _{-0.31}	-0.71 ^{+0.09} _{-0.18}
J112549.55+144006.6	171.45646	14.66846	17.4 ^{+4.8} _{-4.2}	3.32 ^{+0.91} _{-0.79}	< 1.34	40.29 ^{+0.10} _{-0.12}	< 40.43	-0.96 ^{+0.00} _{-0.04}
J143310.55+525830.5	218.29404	52.97510	13.4 ^{+3.6} _{-3.9}	5.63 ^{+3.01} _{-2.56}	14.23 ^{+4.94} _{-4.87}	40.82 ^{+0.19} _{-0.26}	41.76 ^{+0.13} _{-0.18}	0.31 ^{+0.29} _{-0.22}
J143312.96+525747.3	218.30400	52.96314	3.3 ^{+2.3} _{-1.7}	2.83 ^{+2.37} _{-1.71}	< 10.45	40.52 ^{+0.26} _{-0.40}	< 41.62	-0.71 ^{+0.03} _{-0.29}
J032015.52+412355.1	50.06477	41.39862	104.3 ^{+19.4} _{-19.2}	4.43 ^{+0.79} _{-0.78}	< 2.36	40.05 ^{+0.07} _{-0.08}	< 40.31	-0.71 ^{+0.18} _{-0.15}
J032512.84+003711.6	51.30350	0.61989	< 10.8	1.83 ^{+1.52} _{-1.11}	< 7.19	41.38 ^{+0.26} _{-0.40}	< 42.50	-0.71 ^{+0.03} _{-0.29}
J135740.18+223137.7	209.41768	22.52686	8.6 ^{+3.5} _{-2.8}	1.19 ^{+0.88} _{-0.62}	2.06 ^{+0.97} _{-0.77}	40.39 ^{+0.24} _{-0.32}	41.16 ^{+0.17} _{-0.20}	0.32 ^{+0.35} _{-0.26}
J152131.56+074425.8	230.38150	7.74050	40.4 ^{+9.1} _{-8.4}	2.06 ^{+0.51} _{-0.46}	< 1.72	40.28 ^{+0.10} _{-0.11}	< 40.74	-0.60 ^{+0.19} _{-0.19}
J160003.55+412845.4	240.01480	41.47940	8.7 ^{+3.5} _{-2.9}	1.25 ^{+0.66} _{-0.50}	1.62 ^{+0.86} _{-0.66}	39.85 ^{+0.18} _{-0.22}	40.50 ^{+0.18} _{-0.23}	-0.01 ^{+0.31} _{-0.31}
J092458.83+022519.7	141.24512	2.42214	< 22.0	0.87 ^{+0.43} _{-0.35}	< 1.82	40.38 ^{+0.17} _{-0.22}	< 41.23	-0.72 ^{+0.07} _{-0.28}
J150457.12+260058.5	226.23804	26.01631	68.0 ^{+9.5} _{-9.4}	2.65 ^{+0.38} _{-0.38}	0.40 ^{+0.18} _{-0.15}	40.61 ^{+0.06} _{-0.07}	40.31 ^{+0.16} _{-0.20}	-0.78 ^{+0.07} _{-0.10}
J150501.22+260101.5	226.25512	26.01699	15.1 ^{+4.6} _{-4.0}	0.39 ^{+0.17} _{-0.14}	0.24 ^{+0.15} _{-0.11}	39.78 ^{+0.15} _{-0.19}	40.10 ^{+0.21} _{-0.27}	-0.32 ^{+0.23} _{-0.32}
J123407.84+062922.5	188.53273	6.48972	6.4 ^{+3.1} _{-2.4}	2.95 ^{+1.55} _{-1.20}	< 3.44	41.02 ^{+0.18} _{-0.23}	< 41.61	-0.69 ^{+0.09} _{-0.31}
J151022.87+074304.2	227.59545	7.71802	4.3 ^{+2.6} _{-1.9}	3.15 ^{+1.69} _{-1.43}	< 4.82	40.50 ^{+0.19} _{-0.26}	< 41.22	-0.84 ^{+0.00} _{-0.16}
J211706.99-064327.9	319.27920	-6.72440	112.0 ^{+11.2} _{-11.1}	20.79 ^{+2.55} _{-2.52}	8.84 ^{+1.50} _{-1.50}	40.95 ^{+0.05} _{-0.06}	41.11 ^{+0.07} _{-0.08}	-0.33 ^{+0.09} _{-0.10}
J140343.63+292045.3	210.93175	29.34581	4.3 ^{+2.6} _{-2.0}	< 7.20	3.73 ^{+2.38} _{-1.92}	< 41.18	41.43 ^{+0.21} _{-0.31}	0.45 ^{+0.50} _{-0.16}
J140345.02+292144.0	210.93768	29.36215	14.4 ^{+4.1} _{-3.8}	6.45 ^{+2.68} _{-2.25}	8.75 ^{+3.32} _{-3.16}	41.14 ^{+0.15} _{-0.19}	41.81 ^{+0.14} _{-0.19}	0.00 ^{+0.26} _{-0.26}
J121354.87+024753.0	183.47858	2.79806	12.7 ^{+4.2} _{-3.6}	1.79 ^{+0.75} _{-0.61}	1.30 ^{+0.77} _{-0.58}	40.72 ^{+0.15} _{-0.18}	41.12 ^{+0.20} _{-0.25}	-0.29 ^{+0.23} _{-0.31}
J032227.88+421626.4	50.61617	42.27400	4.3 ^{+2.6} _{-1.9}	3.23 ^{+2.07} _{-1.66}	< 6.16	40.65 ^{+0.21} _{-0.31}	< 41.46	-0.48 ^{+0.16} _{-0.42}
J160501.37+174632.5	241.25571	17.77569	< 26.0	1.72 ^{+0.83} _{-0.70}	< 1.18	39.98 ^{+0.17} _{-0.23}	< 40.35	-0.78 ^{+0.04} _{-0.22}
J093325.71+340253.1	143.35742	34.04807	8.4 ^{+4.7} _{-4.0}	1.11 ^{+0.50} _{-0.43}	< 0.63	39.62 ^{+0.16} _{-0.21}	< 39.91	-0.92 ^{+0.00} _{-0.08}
J104232.05+050241.9	160.63361	5.04496	606.7 ^{+26.0} _{-25.8}	0.66 ^{+0.22} _{-0.19}	36.20 ^{+1.57} _{-1.55}	39.39 ^{+0.13} _{-0.14}	41.66 ^{+0.02} _{-0.02}	0.96 ^{+0.01} _{-0.01}
J091339.47+295934.7	138.41444	29.99291	56.2 ^{+8.2} _{-8.1}	6.32 ^{+0.95} _{-0.94}	< 1.80	40.21 ^{+0.06} _{-0.07}	< 40.19	-0.92 ^{+0.02} _{-0.07}
J215945.57-002712.0	329.93987	-0.45333	7.6 ^{+3.5} _{-2.9}	3.18 ^{+1.77} _{-1.35}	< 7.33	41.46 ^{+0.19} _{-0.24}	< 42.36	-0.39 ^{+0.32} _{-0.41}
J215947.31-002644.3	329.94696	-0.44544	21.7 ^{+5.3} _{-4.7}	1.51 ^{+1.06} _{-0.76}	8.33 ^{+2.23} _{-1.94}	41.15 ^{+0.23} _{-0.31}	42.42 ^{+0.10} _{-0.11}	0.67 ^{+0.20} _{-0.11}
J082321.67+042220.9	125.84048	4.37237	50.1 ^{+8.4} _{-8.3}	23.03 ^{+4.09} _{-3.74}	< 4.09	41.05 ^{+0.07} _{-0.08}	< 40.84	-0.93 ^{+0.02} _{-0.07}
J080535.00+240950.3	121.39592	24.16397	204.7 ^{+15.2} _{-15.0}	2.85 ^{+0.41} _{-0.40}	6.62 ^{+0.57} _{-0.56}	40.73 ^{+0.06} _{-0.07}	41.63 ^{+0.04} _{-0.04}	0.46 ^{+0.07} _{-0.06}
J135419.95+325547.8	208.58317	32.92994	1244.1 ^{+37.2} _{-36.8}	263.45 ^{+9.21} _{-9.12}	138.58 ^{+7.99} _{-7.91}	41.96 ^{+0.01} _{-0.02}	42.21 ^{+0.02} _{-0.03}	-0.46 ^{+0.03} _{-0.02}
J125939.94+312707.4	194.91642	31.45206	7.3 ^{+3.5} _{-2.9}	0.88 ^{+0.58} _{-0.43}	< 2.74	40.08 ^{+0.22} _{-0.29}	< 41.11	-0.21 ^{+0.47} _{-0.41}
J141503.92+520323.5	213.76633	52.05653	7.7 ^{+3.7} _{-3.1}	< 1.06	< 1.06	< 40.48	< 41.01	-0.02 ^{+0.49} _{-0.40}

NOTE—(1) SDSS names with J2000 coordinates given in the form of "hhmmss.ss+ddmms.s"; (2)-(3) Centroid position of the X-ray counterpart; (4) Observed net counts in 0.5-8 (*F*) keV bands; (5)-(6) Observed photon flux in 0.5-2 (*S*) and 2-8 (*H*) keV bands, in units of 10^{-6} ph cm $^{-2}$ s $^{-1}$; (7)-(8) 0.5-2 and 2-10 keV unabsorbed luminosities, in units of erg s $^{-1}$; (9) Hardness ratio between the 0.5-2 and 2-8 keV bands.

Table 3. X-ray detection rate of different samples

Sample	Sample size	# of detection	<i>F</i> band	<i>S</i> band	<i>H</i> band	detection rate
(1)	(2)	(3)	(4)	(5)	(6)	(7)
AGN pairs	134	75	72	69	47	56% ± 6%
Single AGNs	115	66	60	58	36	57% ± 7%
SFG pairs	134	23	22	20	6	17% ± 4%
SFG pairs (stellar mass > 10 ⁹ M _⊙)	78	16	16	14	5	21% ± 5%
AGN pairs ($r_p \gtrsim 10$ kpc)	94	44	41	40	25	47% ± 7%
AGN pairs ($r_p \lesssim 10$ kpc)	40	31	31	29	22	78% ± 14%
AGN pairs ($L_{2-10} > 10^{41}$ erg s ⁻¹)	134	36	36	33	36	27% ± 4%
Single AGNs ($L_{2-10} > 10^{41}$ erg s ⁻¹)	115	27	27	23	27	23% ± 5%
SFG pairs ($L_{2-10} > 10^{41}$ erg s ⁻¹)	134	2	2	1	2	1% ± 1%
(detection limit > 10 ^{41.2} erg s ⁻¹)						
AGN pairs	114	65	63	60	40	57% ± 7%
Single AGNs	94	59	54	53	32	63% ± 8%
SFG pairs	90	20	20	17	6	22% ± 5%

NOTE—(1) Samples; (2) Number of nuclei in different samples; (3) Number of detected nuclei in X-ray for different samples; (4)-(6) Number of detected nuclei in the *F*, *S* and *H* X-ray band, respectively; (7) X-ray detection rate.**Table 4.** X-ray Luminosity of the three newly confirmed kpc-scale AGN pairs

Name	r_p	Counts	$\log L_{0.5-2}$	$\log L_{2-10}$	SFR	$\log L_{0.5-2}^{\text{SF}}$	$\log L_{2-10}^{\text{SF}}$
(1)	(2)	(3)	(4)	(5)	(6)	(7)	(8)
J1450-0002a	2.3	57.6 ^{+8.1} _{-8.0}	40.86 ^{+0.07} _{-0.07}	40.63 ^{+0.14} _{-0.16}	0.11 ^{+0.45} _{-0.11}	38.71 ^{+0.69} _{-1.37}	38.76 ^{+0.69} _{-1.37}
J1450-0002b	2.3	5.5 ^{+3.1} _{-2.5}	< 40.32	< 40.67	0.02 ^{+0.10} _{-0.02}	37.85 ^{+0.87} _{-1.31}	37.90 ^{+0.87} _{-1.31}
J0858+1822a	3.3	15.7 ^{+4.7} _{-4.0}	40.58 ^{+0.11} _{-0.13}	< 40.78	3.55 ^{+8.31} _{-2.62}	40.20 ^{+0.52} _{-0.58}	40.25 ^{+0.52} _{-0.58}
J0858+1822b	3.3	13.6 ^{+4.4} _{-3.7}	40.49 ^{+0.12} _{-0.14}	< 40.91	3.46 ^{+9.05} _{-2.88}	40.19 ^{+0.56} _{-0.78}	40.24 ^{+0.56} _{-0.78}
J1414-0000a	4.9	1198.5 ^{+36.6} _{-36.2}	41.50 ^{+0.02} _{-0.02}	42.21 ^{+0.02} _{-0.02}	0.27 ^{+0.77} _{-0.24}	39.08 ^{+0.59} _{-1.03}	39.12 ^{+0.59} _{-1.03}
J1414-0000b	4.9	562.2 ^{+25.1} _{-24.9}	41.42 ^{+0.02} _{-0.03}	41.67 ^{+0.03} _{-0.03}	3.54 ^{+4.94} _{-2.12}	40.20 ^{+0.38} _{-0.40}	40.25 ^{+0.38} _{-0.40}

NOTE—(2) Projected physical separation of AGN in each pair, in units of kpc; (3) Observed net counts in 0.5-8 keV bands; (4)-(5) 0.5-2 (*S*) and 2-10 keV bands unabsorbed luminosities, in units of erg s⁻¹; (6) Fiber star formation rate, in units of M_⊙ yr⁻¹, given by the MPA-JHU DR7 catalog inferred from D_n(4000); (7)-(8) 0.5-2 (*S*) and 2-10 keV bands X-ray luminosities due to star formation.